Spatiotemporal Dispersion Compensation for a 200-THz Noncollinear Optical Parametric Amplifier

William P. Carbery,[1] Laurie A. Bizimana,[1] Matthew S. Barclay, ,[2] Nicholas D. Wright, ,[2] Paul H. Davis, ,[2,3] William B. Knowlton, ,[2,4] Ryan D. Pensack ,[2] Paul C. Arpin ,[5] and Daniel B. Turner[1,2,a)]

[1)] *Department of Chemistry, New York University, New York NY 10003, USA*

[2)] *Micron School for Materials Science and Engineering, Boise State University, Boise ID 83725, USA*

[3)] *Center for Advanced Energy Studies, Idaho Falls, ID 83401, USA*

[4)] *Department of Electrical & Computer Engineering, Boise State University, Boise, ID 83725, USA*

[5)] *Department of Physics, California State University, Chico, Chico, California 95929, USA*

(Dated: 9 January 2024)

A noncollinear optical parametric amplifier (NOPA) can produce few-cycle femtosecond laser pulses that are ideally suited for time-resolved optical spectroscopy measurements. However, the nonlinear-optical process giving rise to ultrabroadband pulses is susceptible to spatiotemporal dispersion problems. Here we detail refinements, including chirped-pulse amplification (CPA) and pulse-front matching (PFM) that minimize spatiotemporal dispersion and thereby improve the properties of ultrabroadband pulses produced by a NOPA. The description includes a rationale behind the choices of optical and optomechanical components, as well as assessment protocols. We demonstrate these techniques using a 1 kHz, second-harmonic of Ti:sapphire pump configuration, which produces ∼5-fs duration pulses that span from about 500 to 800 nm, a bandwidth of about 200 THz. To demonstrate the utility of the CPA-PFM-NOPA, we measure vibrational quantum beats in the transient–absorption spectrum of methylene blue, a dye molecule that serves as a reference standard.

---

[a] Electronic mail: danielturner926@boisestate.edu

I. INTRODUCTION

Pioneering developments in nonlinear optics since the 1990s have led to the advancement of the noncollinear optical parametric amplifier (NOPA),[1–7] a coherent light source that can produce optical pulses in the visible spectral region having durations as short as 5 femtoseconds. Because of the very short durations, these pulses are useful for time-resolved spectroscopy measurements requiring the highest temporal resolution, in particular measurements of quantum beats. In the spectral domain, these pulses have ultrabroad (∼200 THz) bandwidths and are, therefore, ideally suited to two-dimensional electronic spectroscopy (2D ES) measurements of condensed-phase samples. Representative reports that incorporated measurements conducted with NOPAs include transient–absorption studies of photochemical reactions[8–10] and 2D ES studies aimed at understanding energy transfer in photosynthesis.[11–13]

Because a NOPA can produce ultrabroadband laser pulses having very few optical cycles, heterogeneity across the spectrum—'chirp'—for any of the spatial (x), angular ($\boldsymbol{k}$), temporal (t), and spectral (ω) variables limits the efficacy of the device for femtosecond measurements because chirp can induce distortions in measured spectra.[14–21] The dispersion variables are coupled during the amplification process,[22] which makes the task of producing chirp-free pulses challenging. Researchers have studied how the dispersion variables can be minimized by evaluating anamorphic focusing of the pump pulses,[23] pulse-front matching,[24] chirped pump pulses,[25] temporally and angularly dispersed pump pulses,[26,27] angularly dispersed seed pulses,[28] two-color pumping,[29] dispersion compensation of the white-light seed pulse,[6,30] and improving focusing conditions and parasitic processes.[31–33] Review articles provide guidance on NOPA design in terms of these dispersion variables.[34,35] The wide range of spatiotemporal dispersion issues that must be managed leads to many possible pitfalls, which limits the wider adoption of the NOPA. This is unfortunate because NOPAs, such as the one detailed in this report, can produce beams having an excellent spatial mode with a shot-to-shot stability limited only by the source laser fluctuations, and NOPAs can be implemented over wide wavelength ranges.

This contribution details a NOPA design that minimizes chirp to produce few-cycle pulses that are ideal for femtosecond time-resolved spectroscopy measurements. A key aim is to elaborate the design and implementation methods comprehensively. The NOPA detailed here is similar to one presented previously,[30] with the following differences: dispersion compensation in the pump arm to maximize power and stability, optics to optimize the spatial profile of the seed, a prism in the pump arm to match the pulse-front tilt of the pump to the seed, and optics to correlate input pointing changes for the pump and seed beams. Some of these individual ideas have been reported, but never in this advantageous combination. We provide protocols for assessment of the alignment and stability. Finally, we present a measured femtosecond transient–absorption spectrum to demonstrate the utility of the chirped-pulse amplification, pulse-front matched (CPA-PFM) NOPA.

II. THEORETICAL

Before addressing the practical details of design and optimization, it is helpful to elaborate two theoretical aspects that give rise to many of the challenges associated with NOPAs. The first is the pernicious problem of material dispersion compensation, and the second is the coupled spatiotemporal dispersion arising from beam propagation through dispersive media.

A. Material Dispersion Compensation

The wavelength dependence of the index of refraction for a material can be quantified by its Sellmeier equation, $n(\lambda)$, which is ultimately responsible for many of the challenges associated with the design and construction of optical systems,[36,37] especially a NOPA. Achieving a transform-limited pulse duration and concomitant flat spectral phase profile requires an understanding of the various sources of dispersion in the optical system.[38] The group velocity dispersion (GVD) and third-order dispersion (TOD) functions for a material are given by

$$\mathrm{GVD}(\lambda) = \frac{\lambda^3}{2\pi c^2}\frac{d^2 n(\lambda)}{d\lambda^2} \tag{1a}$$

$$\mathrm{TOD}(\lambda) = -\frac{\lambda^4}{4\pi^2 c^3}\left(3\frac{d^2 n(\lambda)}{d\lambda^2} + \lambda\frac{d^3 n(\lambda)}{d\lambda^3}\right), \tag{1b}$$

where we have retained the wavelength dependence of the index of refraction. Although it is possible to carry out the differentials in Eqns. (1) for a given phenomenological Sellmeier equation to form lengthy analytic expressions, the differences between reported coefficient values for a material under identical conditions indicate that the error of the Sellmeier coefficients is similar to or larger than the error arising from a numeric approximation of the derivatives. Therefore we compute the second-order and third-order derivatives using central-difference approximation formulae[39] of order $O(\delta\lambda^2)$. We display computed dispersion curves in FIG. 1 for six common materials including the ordinary axis of β-barium borate (BBO), a birefringent crystal that serves as a common amplification medium. While air seems insignificant because it has a GVD that is orders of magnitude less than other materials, many NOPAs—and spectrometers that use NOPAs—have several meters of path-length, which can make air the largest source of GVD.

It is useful to consider values at all relevant wavelengths because a common approach is to use commercial dispersion-compensating mirror pairs (DCMPs) designed specifically for UV fused silica to compensate for the dispersion induced by all of the materials in the NOPA and subsequent time-resolved spectrometer. To evaluate the efficacy of this approach, in FIG. 2 we present the dispersion ratios for four common materials—sapphire, air, SF10, and BBO—by first normalizing each dispersion curve and then dividing by the dispersion curve for UV fused silica. The results show that sapphire and UV fused silica have similar dispersive properties, with a correspondence of 97% or better across the spectrum. By contrast, UV fused silica has a distinct dispersion relative to BBO, SF10, and air, dipping to about 75%. Hence, using DCMPs designed purely for UV fused silica may not adequately compensate the dispersion of ultrabroad bandwidth pulses that propagate through many materials.

B. Spatiotemporal Dispersion During Amplification

The previous section describes the effect of material dispersion on a broadband pulse after it propagates through a material, where the angle of incidence was ignored. If a broadband pulse is incident on a material at a non-perpendicular angle, then Snell's law needs to be combined with the wavelength-dependent index of refraction to yield

$$\theta_2(\lambda) = \sin^{-1}\left(\sin(\theta_1)\frac{n_1(\lambda)}{n_2(\lambda)}\right), \tag{2}$$

where now each wavelength of the transmitted beam has a distinct refraction angle. This is known as angular dispersion and can introduce pulse front tilt and other distortions to the spatiotemporal profile of the pulse. Managing angular dispersion is an important NOPA design principle because in a NOPA, one or more beams has a non-normal angle of incidence relative to the surface of the amplification crystal.

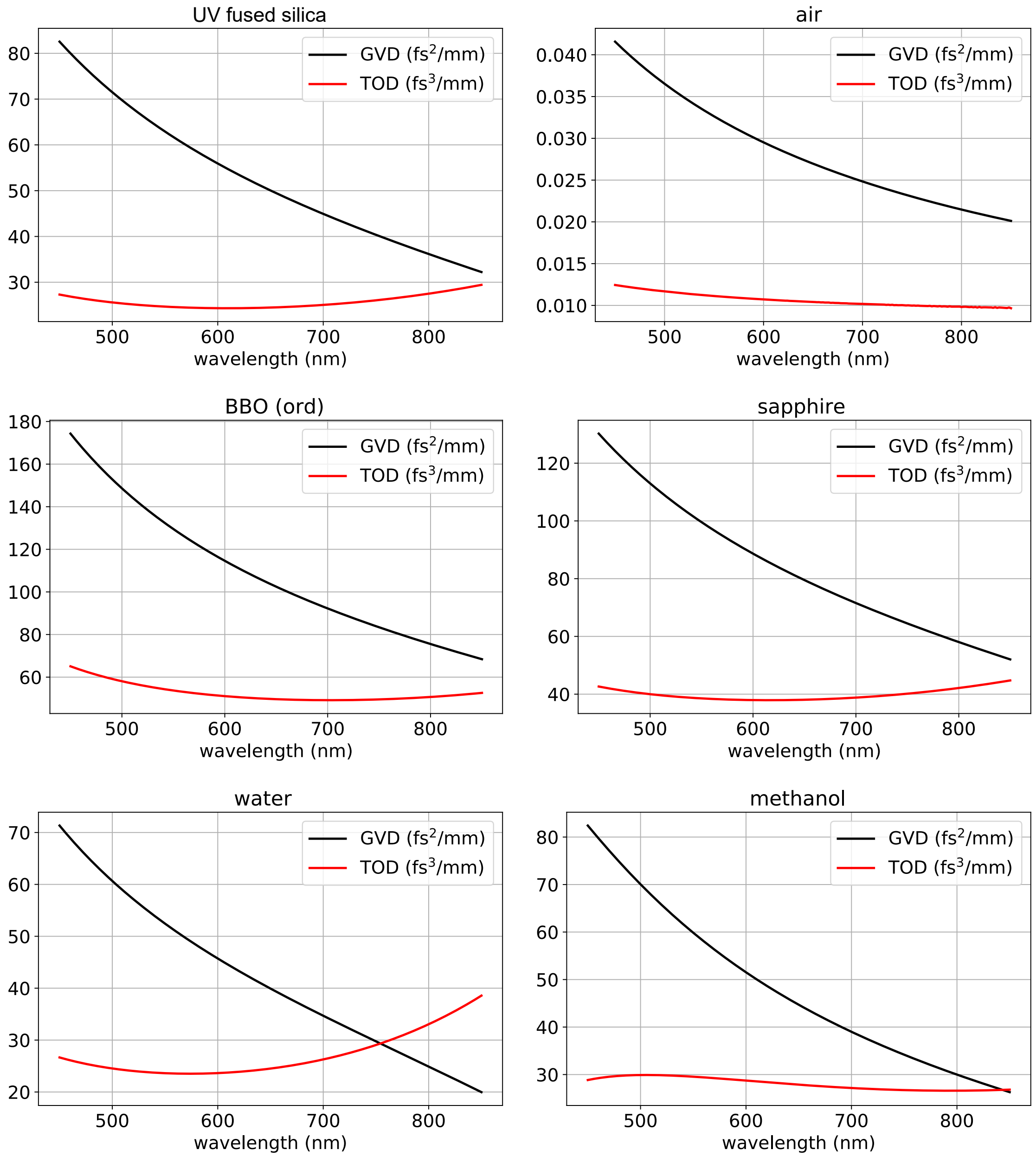

FIG. 1: Second-order (GVD(λ)) and third-order (TOD(λ)) dispersion curves for six common materials computed using Eqns. (1) with $\delta\lambda = 1$ nm. The water temperature was set to 21 °C. Air can be the largest source of GVD when pathlengths are several meters.

In an optical amplifier such as a collinear OPA or NOPA, the phase-matching condition describes the portions of the supercontinuum spectrum that will be amplified by the pump beam during the sum-frequency ($\chi^{(2)}$) process. The phase-matching condition states[34,40] that amplification will only occur with appreciable efficiency when $\Delta k = |\boldsymbol{k}_p - \boldsymbol{k}_s - \boldsymbol{k}_i| = 0$,

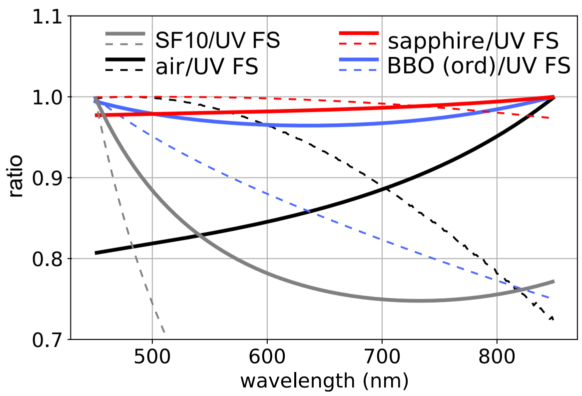

FIG. 2: Ratio of normalized material dispersion relative to UV fused silica. Thick solid (thin dashed) line represents GVD (TOD) ratios. While sapphire is approximated quite well by UV fused silica, the other materials are approximated poorly.

where p, s, and i refer to the pump, signal, and idler beams, respectively. During the amplification process, Δk explicitly relates to the wavevector of the electric field, and reformulating the phase-matching condition in terms of frequency and refractive index yields

$$\omega_p(n(\omega_p) - n(\omega_s)) + \omega_i(n(\omega_s) - n(\omega_i)) = 0, \tag{3}$$

where we used energy conservation, $\omega_s = \omega_p - \omega_i$. Most isotropic materials have positive dispersion, $\partial n(\omega)/\partial\omega > 0$. For the typical condition of $w_i < w_s < w_p$, then $n(\omega_p) - n(\omega_s) > 0$ and $n(\omega_s) - n(\omega_i) > 0$ and there exists no valid solution to Eqn. (3). Birefringent media—such as the ubiquitous BBO crystal—have two distinct refractive indices, one for the ordinary axis, $n_o(\lambda)$, and the other for the extraordinary axis, $n_e(\lambda)$. By aligning the polarization of the pump beam such that it encounters the higher refractive index while the signal and idler are polarized along the lower refractive index, the phase-matching condition can be satisfied. Adding an extraordinary and ordinary refractive index for this type I phase matching to the phase-matching condition yields

$$n_e(\omega_p)\omega_p - n_o(\omega_s)\omega_s - n_o(\omega_i)\omega_i = 0, \tag{4}$$

and the correct matching of the pump and signal beams is dependent on the crystal cut angle, θ_{xtal}, because the overlap of the pump and supercontinuum inside the BBO crystal depends on the projection of the pump pulse onto n_o. Due to Eqn. (2), it is important to distinguish the external pump-tilt angle, θ_{pt}, from the pump-tilt angle internal to the crystal,

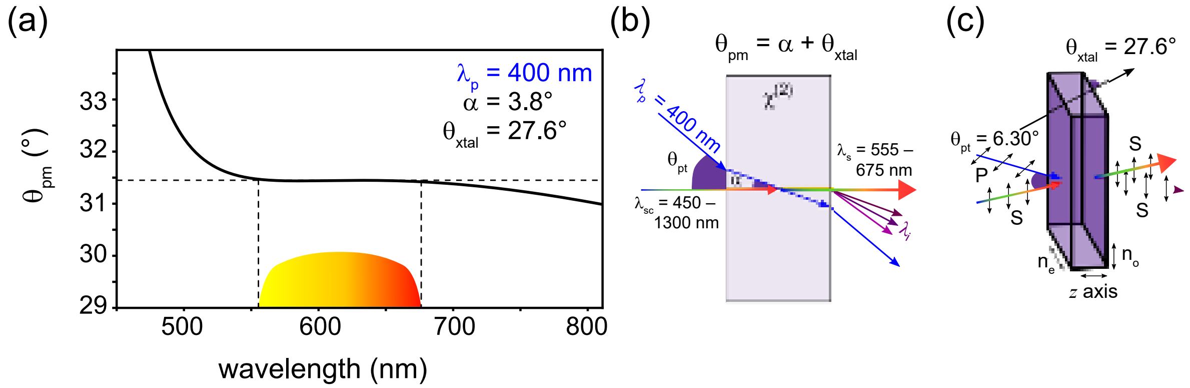

FIG. 3: (a) Representative noncollinear optical parametric amplifier (NOPA) phase-matching curve. (b) Noncollinear geometry conditions. λ_{sc}, λ_{p}, and λ_{s} indicate the sapphire supercontinuum, pump, and signal spectra, respectively. The pump-tilt angle, θ_{pt}, represents the external difference between the pump and supercontinuum pulses, which, after refraction at the air/crystal interface, becomes the internal angle, α. The phase-matching angle, θ_{pm}, combines α and the crystal cut angle, θ_{xtal}. P and S indicate polarization of beams relative to plane of crystal surface. (c) 3D view.

α. For noncollinear beams, the total phase-matching angle[34,40] is given by $\theta_{\mathrm{pm}} = \theta_{\mathrm{xtal}} + \alpha$ such that

$$\omega_p \left(\frac{\sin^2(\theta_{\mathrm{pm}})}{n_e^2(\omega_p)} + \frac{\cos^2(\theta_{\mathrm{pm}})}{n_o^2(\omega_p)} \right)^{-1/2} = n_o(\omega_s)\omega_s \cos(\alpha) + n_o(\omega_i)\cos(\beta), \tag{5}$$

where

$$\beta = \arcsin\left(\sin(\alpha) \frac{n_o(\omega_s)\omega_s}{n_o(\omega_i)\omega_i} \right). \tag{6}$$

The solution to Eqn. (5) can be found numerically for a given pump frequency and specific crystal-cut angle. FIG. 3 shows one such phase-matching curve; in this representative example, the pump wavelength is 0.4 μm and $\alpha = 3.8°$ to yield phase matching from 555 nm to 675 nm, a bandwidth of about 100 THz. This result accounts for the phase-matching process, but it neglects several important physical effects arising from beam propagation through a dispersive medium.

During an ideal amplification process, the pump and seed beams would have perfect spatial and temporal overlap as the fields propagate through the amplification medium. However, the wavelength dependence of the refractive index induces temporal walk-off between the seed and pump beams during the amplification process, even when beams are

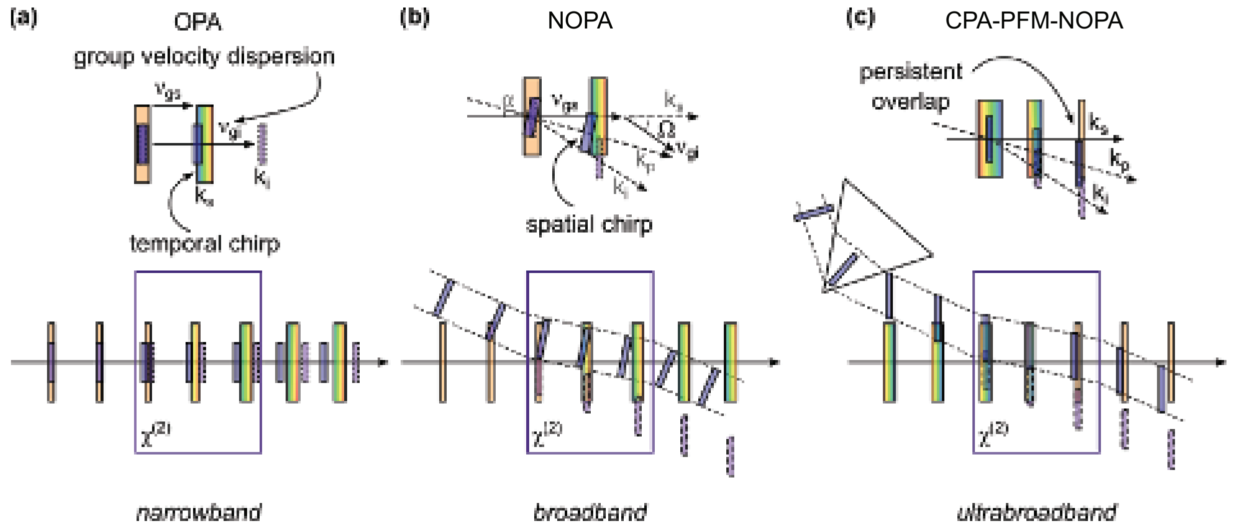

FIG. 4: Schematic illustrations comparing the geometry of a (a) collinear OPA, (b) conventional NOPA, and (c) chirped-pulse amplification (CPA) and pulse-front matching (PFM) NOPA. Each advancement improves the spatial and temporal overlap of the pump (k_p, purple, solid line), signal (k_s, orange/multicolored, solid line), and idler (k_i, purple, dashed line) pulses inside the amplification crystal to maximize bandwidth and reduce spatiotemporal dispersion.

collinear and the crystal thickness is 1 mm or less. FIG. 4 presents schematics depicting the effects of temporal walk-off and spatiotemporal dispersion on the amplification process in three cases by displaying timelines for each laser pulse as it propagates through the amplification material. In all panels, the box marked with $\chi^{(2)}$ represents the amplification medium, the small purple rectangle represents the pump, the larger rectangle that changes between orange and a rainbow represents the seed/signal, and the purple rectangle with dashed border represents the idler. Panel (a) depicts an OPA, in which the pump, signal, and idler beams are collinear, and hence there are no spatial distortions, assuming perfect alignment. However, there is a large mismatch in the group velocities of the signal (ν_{gs}), pump (ν_p), and idler (ν_{gi}), and this mismatch causes rapid, substantial temporal walk-off among the beams. The walk-off and the geometry limit the amplification bandwidth of the OPA for crystal thicknesses that yield usable amount of gain.

The conventional NOPA design of panel (b) depicts that—when the pointing of the pump beam is changed to have an internal angle α relative to the signal beam and a concomitant internal angle Ω relative to the idler beam—there is less temporal walk-off. Furthermore, using Eqn. (5) shows that this design can produce broader phase matching relative to an OPA. However, the angled pump beam induces spatial chirp on the signal beam from two sources. The first source is that a focused pump beam necessarily contains multiple angles of incidence, causing the amplification to be heterogeneous at the overlap of the pump and seed pulses. Later in this work, we quantify the *distribution* of pump incidence angles such that the higher and lower angles are $\alpha \pm \Delta\alpha$, respectively. While panel (b) of FIG. 4 does not depict this issue for simplicity, it does nevertheless occur in the laboratory and even led one group to construct a NOPA in which the pump beam was not focused to the BBO crystal.[41] A second contribution to the spatial chirp—which is depicted in panel (b)—is that, like the OPA case, the continuum seed pulse stretches temporally as it propagates through the amplification medium. Because the pulse fronts are not parallel,[42,43] there is a time and spatial dependence to the amplification process. Pump pulses at higher incidence angles only encounter a fraction of the overall seed bandwidth when both pulses overlap in space and time. These two issues give rise to the spatial dependence of the amplification process and strong observable spatiotemporal distortions. Finally, both panels (a) and (b) depict a perfectly input seed pulse that has perfect temporal compression when first incident on the amplification medium. This is generally not the case due to propagation through the supercontinuum medium, air, and in many cases, lenses, whereas panel (c) shows a seed pulse that has been intentionally chirped to pre-compensate for the dispersion it will experience in the amplification medium, as described in greater detail below.

To minimize the spatiotemporal distortions of the amplification process while retaining the noncollinear geometry that reduces the temporal walk-off, two adjustments are needed. Panel (c) depicts the addition of chirped-pulse amplification (CPA) and pulse-front matching (PFM). We note that the term OPCPA is typically used to describe parametric amplification with a stretched signal pulse to improve the temporal overlap with a long pulse pump laser for high-power OPAs.[44] The intent here is similar—we modify the chirp of the signal pulse to improve temporal overlap with the pump throughout the nonlinear crystal. Chirped-pulse amplification involves pre-compression of the white-light seed pulse such that it has a much shorter duration than the pump beam at the point of maximum overlap in the amplification medium, roughly midway through the material. An alternative strategy to reduce temporal walk-off that has proven successful is to chirp the pump pulse by adding material to the pump-pulse arm.[45] In our attempts, the UV fused silica material placed in the pump arm produced some self-phase modulation that negatively affected the amplification process and stability. Perhaps other material types would have yielded more robust results. Both strategies reduce the temporal walk-off significantly. Pulse-front matching refers to the action of tilting the pulse front of the pump beam using a prism such that the wavefront is parallel to the crystal. The tilted pulse front reduces the spatial dependence of the amplification process and thereby allows for more homogeneous amplification. In our experience, these enhancements also increase the amplification bandwidth and, furthermore, allow for coarse spectral control. This, consequently, can yield a shorter pulse duration as well as enable measurements of coupling between energy levels that are farther apart in the spectrum. In this work, we demonstrate that the CPA-PFM NOPA can yield ultrabroadband pulses free of the spatio-spectral distortions that are produced in a conventional NOPA.

III. METHODS

In this section we detail the CPA-PFM NOPA design, assessment protocols for key properties, and guidance for how to maximize stability and minimize distortions.

A. CPA-PFM NOPA Design

FIG. 5 presents the laboratory implementation of the CPA-PFM NOPA, which is pumped by a commercial 1-kHz Ti:sapphire amplified laser ($\sim$150 fs duration, $\lambda_0 \sim 800$ nm). Reflective optics used for the fundamental beam as well as the second-harmonic beam have broadband dielectric coatings for appropriate polarization conditions, and all optics in the seed beam after supercontinuum generation have a protected-silver or other metallic coating. Throughout the discussion, z indicates the propagation direction of a given beam. The footprint of the enclosure is 48 cm by 99 cm. The first optic (BS) is a UV fused silica window (1" diameter, 3 mm thickness, anti-reflection coated on the back surface) that reflects about 3% of the input beam to be used for supercontinuum generation. The input polarization can be either horizontal or vertical because both the seed and pump arms have half-wave plates. The transmitted beam will serve as the pump.

1. Supercontinuum Arm

In the reflected arm, the beam transmits through a fixed neutral-density filter (ND) for homogeneous intensity reduction and then a half-wave plate (HWP; Tower Optical Z-25.4-A-.500-C-800) and an anti-reflection coated polarizer (Pol; Thorlabs GL15-B) for fine intensity control. The polarizer is set to transmit vertical polarization so that the pump and seed beams of the NOPA can be set to fixed heights and to intersect horizontally in the amplification crystal. The waveplate/polarizer combination leads to a more homogeneous intensity distribution relative to the more-commonly used variable ND filter.[3,30] Having a spatially homogeneous fundamental beam simplifies the generation of a spatially homogeneous supercontinuum seed beam. The attenuation amount of the ND filter is chosen to reduce the beam intensity such that the optimum HWP rotation angle will be approximately midway between a minimum and maximum, yielding the finest possible intensity control. The beam transmits through an iris (TI; Thorlabs ID12) set to a diameter of approximately 4 mm. The iris is fixed to a translating lens mount (Thorlabs LM05XY) for fine adjustment of an optimal central region of the larger fundamental beam. The transmitted beam is then focused by a lens (L1; f=50 mm; uncoated) mounted on a 2D manual translation stage and focused to a 2-mm thick sapphire plate (saph) for continuum generation. The sapphire window is held in a manual rotation mount (Thorlabs RSP1) with the focused beam set to be off-center so that if the crystal becomes dirty or damaged, one can simply rotate to an undamaged spot without having to perform any realignments.

Most prior NOPA designs incorporate a lens or a 0° spherical mirror used at a non-zero angle to collimate the supercontinuum seed beam and then focus it to the amplification crystal. These optics are straightforward to align, however, both will introduce undesirable spatiotemporal distortions to the broadband beam, and in the case of the lens, additional unwanted temporal dispersion. We use a 90° off-axis parabolic mirror (OAPM, f=20 mm, Newport 50328AL) because it does not introduce aberrations to the spatial mode or temporal dispersion. The short focal length keeps the beam as small as possible, which, as we detail in a later section, is an important design consideration. The surface roughness of an OAPM is the primary cause of scatter, and this specific optic has the smallest specification value we could source commercially, 25 Å. A potential disadvantage to using an OAPM is alignment difficulty. OAPMs have 6 degrees of freedom that are coupled to each other and

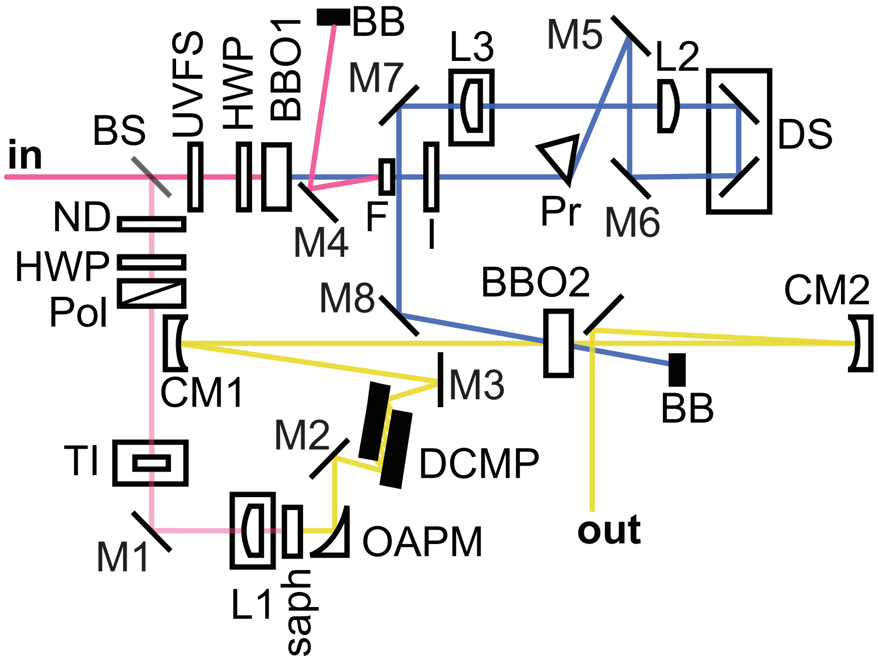

FIG. 5: Schematic of the CPA-PFM-NOPA, containing a beamsplitter (BS), a neutral-density filter (ND), half-wave plates (HWP), a polarizer (Pol), a translatable iris (TI), mirrors (M), lenses (L), a sapphire window (saph), an off-axis parabolic mirror (OAPM), a dispersion-compensating mirror pair (DCMP), curved mirrors (CM), β-barium borate crystals (BBO), a UV fused silica window (UVFS), a bandpass filter (F), iris (I), beam blocks (BB), a prism (Pr), and a delay stage (DS). The fundamental input beam (red) yields a weak supercontinuum beam (yellow) and a strong pump beam (blue). Amplification in BBO2 yields the output signal beam (yellow).

therefore have a reputation as being difficult to align. To simplify alignment tremendously, the positional and angular degrees of freedom can be decoupled from each other by introducing an additional flat mirror (M2) after OAPM. Our OAPM is fixed, using a custom adapter plate, to a manual three-axis positioner (OptoSigma TAM-655SRLUU) that allows for fine alignment of the location of the optic. We include a computer-aided design .step file for the custom adapter plate as Supplementary Material. The angles of OAPM are aligned by hand using the custom adapter plate; we estimate an angular tolerance of better than ±2° can be achieved by hand adjustments of the optic while examining the reflected beam in the far field. After OAPM, the beam reflects off M2, which provides fine adjustment of the angular degrees of freedom.

Optimizing the supercontinuum generation process is a key requirement to obtain a stable NOPA. Therefore we elaborate a procedure that typically is successful. The first step is to remove optics L1, saph, and OAPM. We then set TI to select the central region of the fundamental beam, which must be directed by M1 along a row of holes on the optical table and horizontally parallel to the surface of the optical table after mirror M1. We then replace saph and ensure it retroreflects the fundamental beam; the optic should be mounted securely without over-tightening. We then carefully block the beam directly before saph and then insert and align carefully L1, which is not anti-reflection coated so that both back-reflected beams are visible with an IR viewer. Eschewing threaded lens mounts because they induce asymmetric forces that distort an optic, instead we use a nylon or nylon-tipped set-screw–based lens mounts whenever possible. Again, the set screw should be snug without overtightening. Lens L1 has two translational and two angular degrees of freedom. The vertical angle can be optimized adequately by ensuring the optic is flat in the set-screw mount (Thorlabs FMP1). Using the retroreflected beams, one can align both translational and the horizontal angular degree of freedom. The rest of the alignment procedure involves refining the z translation of L1, the setting of the compressor in the Ti:sapphire amplifier, and the two transverse translation dimensions of TI as well as small adjustments to its diameter. The goal is to generate a spatially homogeneous supercontinuum beam at the lowest possible fundamental power; a typical value is $\sim 0.5\ \mu$J/pulse, leading to a supercontinuum beam such as the one displayed as a representative image as the top panel in FIG. 6. There will be some radial dependence to the coloration of the beam, but there should be no localized blotches or discolored regions. An overpumped supercontinuum beam is shown as the middle panel in FIG. 6; this figure also shows the spectra of optimum and overpumped supercontinuum beams in the bottom panel. Observing a red ring outside the main beam is indicative of strong overpumping, which will generate undesired spectral fringes. In the ideal alignment, there is just enough power in the fundamental to overcome the supercontinuum threshold.

Mirror M2 sends the beam into the DCMP, which provides the negative temporal dispersion needed for the CPA process. In a quest to maximize amplification bandwidth, we have evaluated a number of different DCMPs for pre-compression of the supercontinuum seed beam: DCMPs designed to compensate 1.2 mm UV fused silica per double bounce (Laser Quantum - Novanta, formerly Venteon, DCM9) as well as DCMPs designed to compensate 0.5 mm of UV fused silica per double bounce (Layertec 148545), compensate 1.5

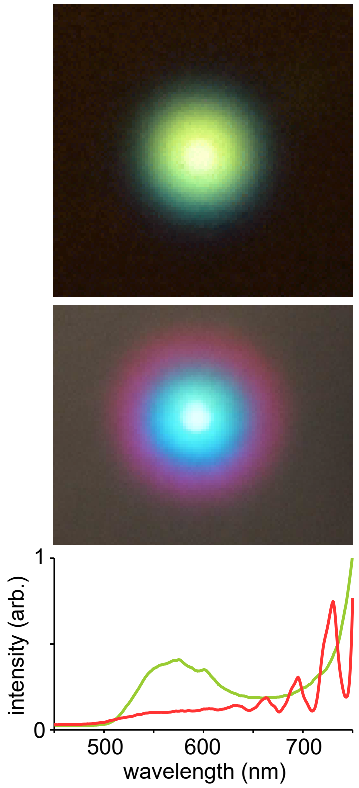

FIG. 6: Photograph of scatter from a white card for typical white-light supercontinuum beam produced at optimum pump power (top) and overpumped (middle). The radial symmetry and lack of red ring are important properties at optimum pump power. (bottom) Spectra of supercontinuum beam produced at optimum (greenish yellow) and overpumped (red) powers.

mm UV fused silica per double bounce (Layertec 174306), and compensate 1 mm of BBO plus 1 mm of sapphire per three double bounces (Layertec 128921). After optimization, the resulting amplified beams were essentially indistinguishable, indicating that coarse control over the dispersion is adequate for optimizing the amplification process. We emphasize two details. The first is that some DCMPs are very sensitive to the angle of incidence, having a tolerance as low as ±0.5°. The wrong angle of incidence can lead to undesired spectral fringes and satellite pulses in the time domain. The second is that DCMPs having multiple reflections are very sensitive to mechanical perturbations, and therefore it is important to mount the DCMPs rigidly to the table without any adjustment knobs using the thickest possible hardware, such as 1.5" diameter posts. Alignment can be accomplished by hand with patience.

After the DCMP, the supercontinuum seed beam is reflected by mirror M3 and sent to an f=750 mm focal length 0° spherical mirror (CM1). Mirror M3 is positioned to make the incidence angle on CM1 as close to zero as possible. At times, we have changed M3 from protected silver to have a protected aluminum or protected gold coating for additional control of the seed spectrum. The long focal length of CM1 is intentional. Inspecting FIG. 4, one can envision that a tightly focused seed beam would lead to a distribution of nonzero angles of incidence on BBO2 that, given Eqn. (2), would lead to significant angular dispersion and subsequent spatio-spectral distortions during the amplification process. Minimizing this potential problem is equivalent to maximizing the Rayleigh range, z_R, which is given by

$$z_R = \frac{4\lambda F^2}{\pi D^2}, \tag{7}$$

where D is the diameter of the beam incident on CM1 and F is the focal length of CM1. Therefore, to maximize z_R and thereby minimize the distribution of angles incident on BBO2, we use the very short focal length OAPM to minimize D and use a very long focal length for CM1 to maximize F. After testing CM1 focal lengths ranging from 250 mm to 2000 mm, we have found that a focal length of 750 mm is the shortest focal length that eliminates detectable angular dispersion. This focal length, given that D ~5 mm, yields z_R ~2 cm. Amplification occurs in BBO2, which has a 1-mm thickness. The cut angle of BBO2 is extremely sensitive to the input wavelength, and we discuss its optimization in a later section. Finally, after amplification, the signal beam is recollimated by CM2 (0° spherical mirror, f=500 mm) used at a small nonzero angle and then picked off by a final mirror. The total propagation distance from saph to BBO2 is about 1.5 meters.

2. Pump Arm

Next, we discuss the pump arm of the CPA-PFM NOPA. The first optic in this arm is a UV fused silica window (UVFS) that has anti-reflection coated surfaces. The thickness is chosen to adjust the dispersion of the fundamental beam to maximize the amount of second-harmonic generated by BBO1. Because the compressor of the Ti:sapphire amplifier is adjusted to optimize the supercontinuum generation, without optic UVFS, the dispersion would lead to sub-optimal SHG, lowering the average intensity and also increasing the shot-to-shot fluctuations.

FIG. 7: Photograph of scatter from a white card for typical NOPA beam to display the near-TEM$_{00}$ spatial mode routinely achieved by the CPA-PFM-NOPA.

Like the supercontinuum arm, the pump arm also contains a HWP for fine control over the power, but no polarizer is needed because second-harmonic generation in BBO1 (7×7 mm size, 1 mm thickness, anti-reflection coated, $\theta \sim 29^\circ$) is polarization sensitive. The cut angle tolerance is 0.1° and is specified according to the precise fundamental wavelength; a different crystal is required when the central wavelength of the fundamental changes more than about 10 nm. A 1-mm crystal thickness will only phase match about 10 nm of bandwidth near 800 nm, which means that one must monitor the spectrum of the second-harmonic beam while optimizing the phase-matching angle. A convenient method to obtain a spatially averaged spectrum of the SHG beam without any focusing optics is to attach a small ($\sim$1 cm^3) block of white foam to the tip of an optical fiber that is set normal to the propagation direction. For a well-aligned crystal, the highest powers will correspond to a symmetric second-harmonic spectrum at a HWP angle that yields maximum power. A bandpass filter (F, Thorlabs FBH400-40) separates the residual fundamental from the desired second-harmonic beam. The residual fundamental is sent by F to a pick-off mirror (M4), which directs the beam to a beam block (BB) that is placed outside the NOPA enclosure to reduce thermal effects that cause drift. The NOPA enclosure minimizes dust, air currents, and thermal gradients.

The beam is then directed through a UV fused silica prism (Pr, 69.06° apex angle, Newport 10SB10) for tilting the pulse front of the pump beam. The prism is set to the minimum-deviation angle. Mirrors M5 and M6 then direct the beam to a pair of mirrors mounted on a manual delay stage. The angular alignment of the two mirrors mounted on the delay stage has a loose tolerance, and we can increase mechanical stability by affixing these mirrors in a single bespoke machined mount, denoted the 'chair'. We include a computer-aided design .step file for the chair as Supplementary Material. The second-harmonic beam then propagates through a telescope composed of two uncoated CaF_2 lenses (L2 and L3, each 1" diameter, f=100 mm) separated by approximately 21 cm. Lens L3 is mounted on a manual translation stage for fine control of the z translation to yield fine control of the focus into the 1-mm thick amplification crystal, BBO2. Mirrors M7 and M8 control the pump overlap angle, $\sim 6°$ external to the crystal (yielding an approximate internal angle of $\sim$3.7°), as well as the overlap of the pump to the seed in the crystal. A key to obtaining an excellent spatial mode is alignment of the two pump lenses using the retroreflected beams. The beam waist at the plane of BBO2 is about 250 μm. Our NOPA uses two lenses as a slightly defocused telescope, rather than a single lens, so that any pointing changes to the input beam due to drift will yield a positive correlation of the pump and seed beams as they interact in BBO2; both beams will move in the same direction, allowing for an amplified output beam with increased long-term stability. As we detail more in a later section, the cut angle of BBO2 is about 27.5°, but must be tailored to the precise wavelength of the fundamental beam and to the desired output spectrum. The BBO2 crystal is set to normal incidence of the seed to eliminate that source of angular dispersion. FIG. 7 shows the output spatial mode that is achieved daily with minimal adjustment.

Our use of a prism was motivated by Kobayashi and coworkers,[41] who, in 2002, used a telescope to ensure the amplification crystal was in an image plane of the tip of the prism. This imaging arrangement produced the desired pulse-front tilt following the sketch in FIG. 4(c). Our implementation of the prism in the Fourier (confocal) plane is complementary to the prior report.

The prism creates angular dispersion $\frac{d\phi_{\text{exit}}}{d\omega}$, where $\phi_{\text{exit}}(\omega)$ is the exit angle from the prism. The initial angular dispersion can be determined from Snell's law applied to the prism interfaces,

$$\frac{d\phi_{\text{exit}}}{d\omega} = -\frac{\lambda_p^2}{2\pi c}\frac{dn}{d\lambda_p}\frac{\sin\alpha_{\text{apex}}}{\cos\left(\phi_{\text{exit}}\right)\cos\left(\sin^{-1}\left(\frac{1}{n}\sin\phi_{\text{enter}}\right)\right)}, \tag{8}$$

where λ_p is the central pump wavelength. Including angular dispersion and allowing for second-order temporal dispersion—assuming a Gaussian spatial and temporal profile—the laser pulse electric-field profile at the exit of the prism can be described in position-frequency space (in the horizontal dimension) as

$$E_{\text{prism}}(\omega, x') = E_0 \exp\left[-\left(\frac{\tau_0^2}{4} + i\frac{\beta}{2}\right)(\omega-\omega_0)^2\right] \exp\left[-\frac{x'^2}{\sigma_x^2}\right] \exp\left[-i\frac{2\pi}{\lambda_p}\frac{d\phi_{\text{exit}}}{d\omega}(\omega-\omega_0)x'\right], \tag{9}$$

where β is the total group delay dispersion, τ_0 is the transform-limited pulse duration, and σ_x is the $1/e^2$ beam intensity radius.

The lenses in the two-lens pump telescope are set such that the distance from the tip of the prism to the first lens of the telescope is equal to the distance from the second lens of the telescope to BBO2. However, the distance between the two lenses in the telescope is deliberately set to a non-collimating value such that the pump pulse focuses near the surface of BBO2. In this geometry, BBO2 is no longer in an image plane of the prism, but in a scaled Fourier plane. In the Fourier plane, the electric field of the pulse can be written as

$$E_{\text{FP}}(\omega, x) \propto E_0 \exp\left[-\left(\frac{\tau_0^2}{4} + i\frac{\beta}{2}\right)(\omega-\omega_0)^2\right] \exp\left[-\frac{\left(x + f_{\text{eff}}\frac{d\phi_{\text{exit}}}{d\omega}(\omega-\omega_0)\right)^2}{\sigma_{x,\text{FP}}^2}\right], \tag{10}$$

where $\sigma_{x,\text{FP}} = \frac{f_{\text{eff}}\lambda_0}{\pi\sigma_x}$ is the CW beam radius in the focal plane. The effective focal length of the two-lens system is given by $f_{\text{eff}} = -(d-f)$, where f is the focal length of each lens and d is the distance from the prism to the first lens and the distance from the second lens to the BBO. The minus sign corresponds to the inverted image of the Fourier plane relative to a single lens system and not a negative focal length lens.

The angular dispersion at the prism plane is mapped as spatial dispersion with a frequency-dependent spatial peak given by $x_0(\omega) = -f_{\text{eff}}\frac{d\phi_{\text{exit}}}{d\omega}(\omega-\omega_0)$. A second form of pulse front tilt arises when both spatial dispersion and temporal dispersion are present.[42,43] This approach has been considered for terahertz generation with tilted pulse fronts.[46] Eqn. (10) can be Fourier transformed to the time domain, and the total pulse front tilt (γ_{FP}) is

$$\tan\gamma_{\text{FP}} = -c\beta f_{\text{eff}}\,\frac{d\phi_{\text{exit}}}{d\omega}\frac{1}{(f_{\text{eff}}\frac{d\phi_{\text{exit}}}{d\omega})^2 + (\frac{1}{2}\sigma_{x,\text{FP}}\tau_0)^2}. \tag{11}$$

In summary, the prism induces angular dispersion with a pulse front tilt, but the telescope arrangement converts that into spatial chirp, which—through standard material dispersion—becomes pulse front tilt in the Fourier plane where BBO2 is placed. The additional complexity is worthwhile because having correlated pump and seed arms in the NOPA significantly increases the long-term robustness of its alignment.

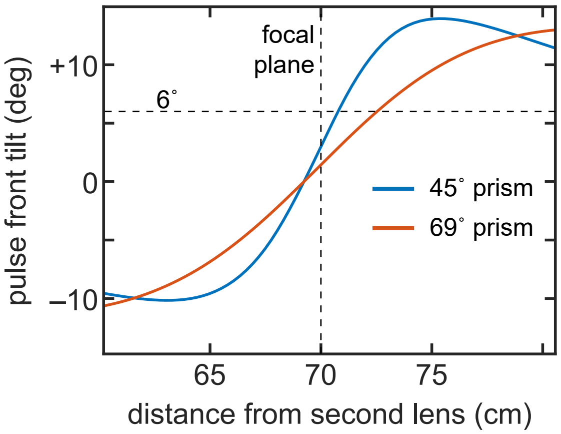

FIG. 8: Calculated pulse-front tilt for two prism apex angles and the conditions described in text.

In our setup, $d = 73$ cm, $f = 10$ cm, $\tau_0 = 64$ fs, $\beta = 1300$ fs^2 for propagation through about 7 mm of fused silica, 7.8 mm of CaF$_2$ (two Thorlabs LA5817 lenses), and 2 meters of air, $\sigma_x = 2$ mm, and the dispersing prism has an apex angle of 69° and is aligned for minimum deviation. This yields a pulse front tilt at the focal plane of $\gamma_{\text{FP}} = 1.9°$. We performed the same calculation for a 45° apex-angle prism, and the result is that $\gamma_{\text{FP}} = 4.0°$ at the focal plane.

Near the focal plane, the pulse front tilt evolves as the beam propagates and generally involves a sum of both forms of pulse-front tilt. We use numerical beam propagation to propagate the beam from the prism, through the two lens system and through the focus, to demonstrate the variation of pulse-front tilt near the focal plane. We propagate the beam through a distance Δz in free space by assuming a quasi-monochromatic beam with central wavelength λ_p and by treating treating each lens with focal length f as a thin phase filter.[47] At each z location, we perform a two-dimensional Fourier transformation to obtain the pulse in the $x - t$ domain, $E(x, t; z)$. In this domain, the pulse front tilt can be found numerically for each z value. We determine the time t_0 that the electric field amplitude peaks at each position x in the spatial extent of the pulse. The pulse front tilt angle γ can be found from

$$\tan\gamma = c\frac{dt_0}{dx}. \tag{12}$$

The numerical beam propagation results are plotted in FIG. 8 for a Brewster angle (69°) prism and a 45° prism. The plot shows the pulse-front tilt as a function of position along the beam propogation direction near the focal plane of the two-lens system. For both prisms, the pulse front tilt varies rapidly through the focal plane effectively creating a "tuning curve" where the pulse front tilt can be optimized by adjusting the relative position of the BBO crystal and the focal plane. One benefit of this approach is that the pulse front tilt can be optimized for a broad range of prism angles and lens choices. In contrast, when the prism output is imaged to the crystal, the optics must be carefully chosen and designed to achieve the correct pulse front tilt.

To test these computational results, we constructed a NOPA that, in turn, used a right-angle prism or a Brewster-angle prism in the pump arm. For the right-angle prism case, we aligned the optic such that the pump beam refracted through one of the 45° corners, and we adjusted the distance between the two pump lenses such that the focus of the pump was quite close to BBO2, about 1–2 cm relative distance. In the other case, the pump beam propagated through the standard corner of the Brewster-angle prism, and the focus of the pump was set further behind BBO2, about 3–4 cm relative distance. The resulting amplified beams were largely indistinguishable from each other, although in some tests the right-angle prism yielded slightly ($\sim$5 nm) more bandwidth. These observations confirm the computational results that pulse-front tilt can be controlled by adjusting the plane of the focus relative to the plane of BBO2.

B. Optimization of Angles

Analogous to a well-aligned interferometer, a well-aligned NOPA can produce an output beam having a spatial mode with circularly symmetric interference rings, also known as an Airy pattern. Achieving an output such as that shown in FIG. 7—in which the pump power was set to yield a mode having just the one central peak of the Airy pattern—requires careful optimization of the noncollinear angles. The crystal-cut and pump-tilt angles that yield the broadest usable output bandwidth depend only on the central wavelength of the input laser, which in turn is governed by the sample. One must identify the central wavelength that yields a NOPA spectrum that maximizes overlap with the sample's absorption and fluorescence spectra. To accomplish this task, one can compute a series of phase-matching calculations at varying pump-tilt angles and prepare a surface plot such as the one shown in the left panel of FIG. 9. By comparing surface plots at varying pump wavelengths, one can identify the optimum internal angle quickly. A surface plot relates the internal angle (α), the crystal cut angle (θ_{xtal}), and output bandwidth at a specified pump wavelength and internal angle width ($\Delta\alpha$). The internal angle width is given by the focusing conditions of the pump beam; in the case of a 0.6 μm wavelength focused by an f=750 mm optic with a 5 mm beam diameter, then $\Delta\alpha \sim 0.12°$.

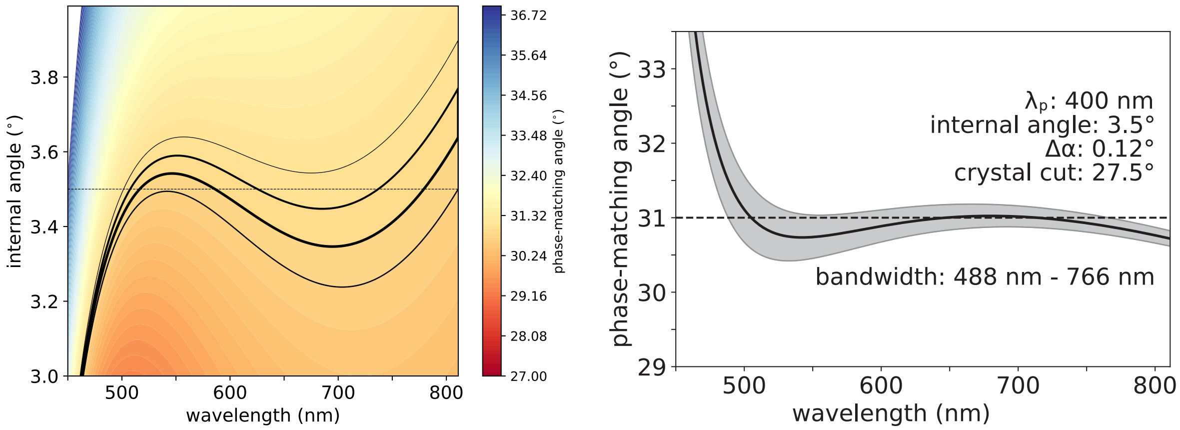

FIG. 9: Phase-matching surface and plot for $\lambda_{\mathrm{p}} = 0.4$ μm that explicitly incorporate $\Delta\alpha$, the distribution of pump-tilt angles caused by the focusing of the pump beam to the amplification medium. Based on the computed amplification bandwidth of 233 THz, one can estimate a pulse duration of 4.5 fs.

Prior NOPA design reports[34,35] and panel (a) of FIG. 3 made the reasonable assumption that the optimal phase-matching angle is the angle that produces the flattest single phase-matching curve. By accounting for nonzero $\Delta\alpha$ arising from focusing of the pump beam, however, the right panel of FIG. 9 shows that phase matching for the greatest bandwidth is actually at lower crystal-cut and internal angles than normally used. We routinely operate the NOPA with lower-than-expected pump tilt and crystal cut angles, which yields ~10 nm of additional bandwidth without incurring spatial chirp or angular dispersion because only the internal geometry of the system has changed.

To summarize, based on the sample spectral properties, we compute phase-matching surfaces for varying pump wavelengths. The surfaces reveal the best choice of amplifier central wavelength, pump-tilt angle, and crystal-cut angle. A few examples are instructive. For phytochromes that absorb in the red, for example,[48] we set the amplifier central wavelength to 820 nm, used a BBO mixing crystal cut to 26.8° and an external (internal) angle of 6.0°

(3.6°) to obtain pulses spanning from about 525 nm to 800 nm. On the bluer side of the spectrum, for rubrene single crystals, we set the amplifier central wavelength to 780 nm and the external (internal) angle to 5.0° (3.0°), for a 27.1° crystal. The resulting pulses spanned from about 460 nm to 550 nm.[49] And, finally, our standard setup shown in panel (b) of FIG. 9 uses an amplifier central wavelength of 800 nm, a 27.5° crystal, and an internal angle of 3.5° yielding pulses spanning from about 490 nm to 770 nm. The external pump-tilt angle has dropped from 6.3° in FIG. 3 to 5.8° in FIG. 9 due to the geometry change. In this configuration, the input pulse energy of 330 μJ yielded 52 μJ of 400-nm beam focused into mixing BBO and 1.1 μJ of 800-nm beam focused into the sapphire. Filtering out the residual fundamental using a 750-nm shortpass optical filter (OptoSigma SHPF-25C-770), the energy of the unamplified supercontinuum was 6.5 nJ and the total output energy was 420 nJ. This is a ∼0.8% conversion efficiency. After pulse compression, in the typical configuration, the amount of energy available for measurements is about 200–300 nJ/pulse.

C. Analysis of Spatio-Spectral Distortions

For a NOPA operating at visible wavelengths, the spatio-spectral dispersion properties can be evaluated with little more than a card with which to view the output beam. Specifically, during alignment, we recommend expanding the output beam by either letting the uncollimated output beam propagate a long distance or by adding a spherical mirror to the output beam to expand its size more quickly than propagation. Using either approach, a user can quickly evaluate the presence of spatio-spectral chirp by looking for changes in color across the beam diameter. Spatial chirp arises when differing frequencies of light are generated at slightly different locations but have parallel wavevectors. By contrast, angular dispersion can arise even when all frequencies are generated in the same location but have non-parallel wavevectors. Either issue will manifest as a frequency-dependent spatial profile; when alignment is very poor, either issue can give rise to a rainbow. The two phenomena can be distinguished by evaluating the beam at a focal plane. If spatial chirp is the issue, all of the colors will focus to the same spot. Angular dispersion, by contrast, leads to a wavelength-dependent focus. One can scan a pinhole through the beam at the focal plane and then assess changes to the color of the diffracted beam on a card placed in the far field.

D. Calibration of Detectors

Because the cut angle of the amplification crystal is so sensitive to the exact wavelength of the pump pulse, one must use great care when measuring the pump wavelength with a spectrometer. Many spectrometers, especially compact USB spectrometers, lose wavelength calibration after only a few months, and we have found shifts of nearly 10 nm are possible. A shift of 10 nm in the fundamental near 800 nm would require a change of BBO crystal-cut angle of 0.4°, which is quite significant compared to the tolerance of 0.1°. The straightforward calibration procedure is a linear fit to several lines from an atomic lamp once it reaches its thermally equilibrated temperature.

For assessment of the spectrum of the amplification process in an ultrabroadband NOPA, it is also important to calibrate the relative-intensity scale of the spectrometer. Most spectrometers report only a relative intensity value that is not corrected for the intensity variations caused by the internal optics as well as the responsivity curve of the detector material, which is most often silicon. We have found that using a broadband light source that acts as a thermal emitter to be a reasonable compromise among cost, reliability, and convenience. One can then generate a correction curve using the calibration lamp.

E. Minimization of Pump Scatter in Time-Resolved Spectroscopy Measurements

An important consideration when conducting time-resolved spectroscopy measurements is to minimize scattering of the laser beams on the sample. The issue is especially problematic for degenerate transient–absorption spectroscopy measurements conducted with ultrabroadband pulses because pump scatter will occur at all wavelengths. The scatter can be on the order of 1% or more, which is a level that obscures many subtle features that are of interest such as coherent quantum beats. Typically one minimizes scatter by ensuring the cuvette windows are undamaged and very clean, as well as filtering liquid samples to remove particulates $\gtrsim 0.2\ \mu$m by using a syringe filter appropriate for the solvent. For aqueous solutions we have found Whatman UNiFLO polyethersulfone #9916-1302 filters to be adequate. For some solvents, another way to reduce scatter from cuvette windows is to remove the cuvette itself by constructing and optimizing a wire-guided jet apparatus.[50–52] These three methods are fairly standard and widely used.

One additional method that seems to be less well-known is to use the optimum material for the cuvette windows, because scatter can arise from the glass itself even with pristine surfaces. The hydroxyl ions present in fused silica material produce intrinsic density fluctuations that cause nonzero pump scatter at visible wavelengths.[53] The hydroxyl ion specification for UV fused silica is ≤ 300 ppm. By contrast, there are some forms of so-called 'IR fused silica' such as Suprasil 300, 3001, and 3002 and Infrasil 301 and 302 that have much lower hydroxyl ion content ($\leq$1 ppm and ≤ 8 ppm, respectively) and, consequently, significantly lower levels of intrinsic scatter. In our experience, the level of scatter from pristine IR fused silica cuvette windows can be so low as to be undetectable. Hence, when possible, one should use IR fused silica windows in cuvettes and demountable liquid cells, an upgrade to our previously reported design.[54]

IV. RESULTS & DISCUSSION

A. NOPA output & compression

Using the methods detailed in Sec. III, we have constructed ultrabroadband NOPAs in multiple laboratories. The characteristics of these NOPAs include: (a) near-TEM$_{00}$ spatial mode such as that shown in FIG. 7 with no detectable angular dispersion, (b) about 200-THz bandwidth, see FIG. 10, (c) shot-to-shot stability of 0.5% RSD with one stage, see FIG. 11, or 0.1% RSD with two stages, (d) pulse duration of ∼5 fs with a flat phase profile, see FIG. 12, and (e) minimal daily alignment required.

We have used several methods to compress ultrabroadband pulses. Based on the analysis of material dispersion in FIG. 1, we purchased DCMPs designed to compensate for 1 m of air per double bounce (Layertec 180504 & 180510). Our multiple attempts at pulse compression using these air DCMPs in addition to a set of UV fused silica DCMPs did not yield distortion-free pulses; often uncompensated third- and higher-order dispersion causes a small pedestal or satellite pulse to persist. Ultimately, we have found that we obtain the best pulses using a combination of UV fused silica DCMPs and a prism-based pulse shaper incorporating, when necessary, a neural-network architecture.[55] The pulse shaper incorporates a prism—rather than the more-common grating—for two reasons. First, the

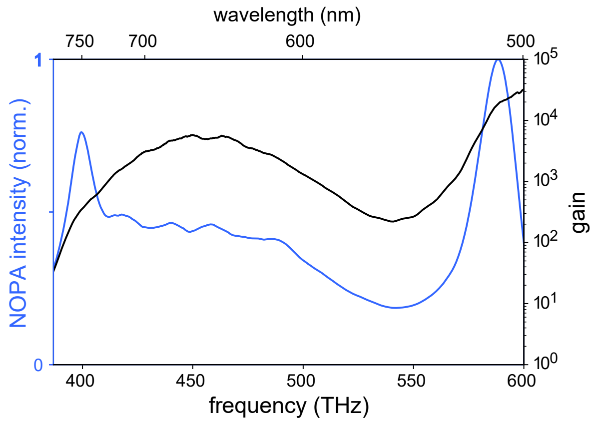

FIG. 10: Spectrum of NOPA output (blue) and parametric gain (black).

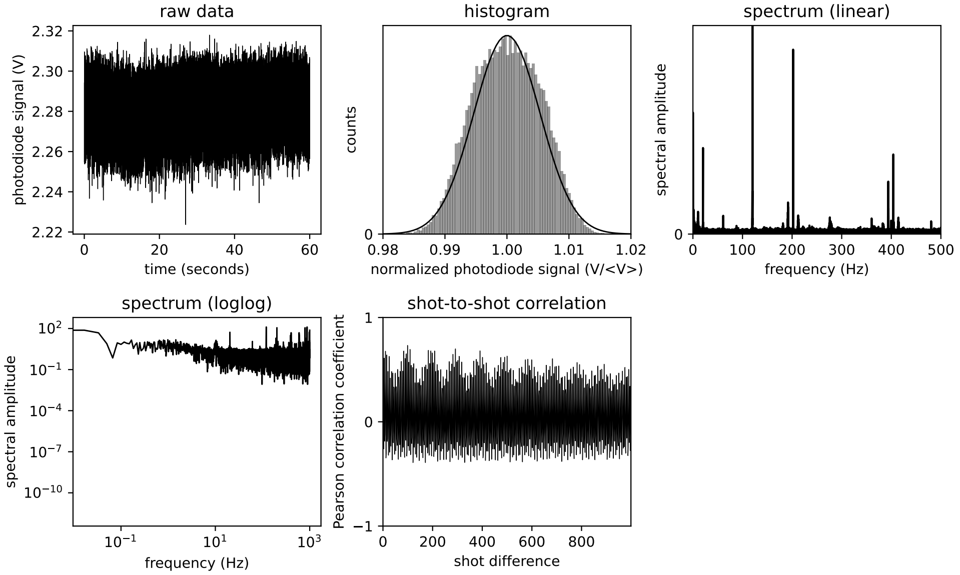

FIG. 11: Statistical analysis of NOPA fluctuations for a representative dataset with RSD of 0.5%.

prism has a much higher efficiency than a grating, and in time-resolved measurements it is helpful to have adequate pulse fluence for generating strong signals. The second advantage is that refraction of the prism material (SF10) has a beneficial wavelength dependence. The prism disperses more in the blues—where the pulse is not well-compressed by the chirped mirrors—and less in the reds—which are already well-compressed by the chirped mirrors. Hence there are more actuators of the deformable mirror available for refining the phase in the bluer region of the spectrum using a prism-based pulse shaper relative to a grating-based pulse shaper. With the pulse shaper, the total distance from `saph` to the sample position is about 10 meters. Without the pulse shaper, the total distance was about 4 meters, however, like a prior work that used only DCMPs for compression,[30] the satellite pulses were slightly larger and phase profile was not as flat relative to those attainable with a pulse-shaping setup, despite the decreased dispersion due to reduced pathlength in air.

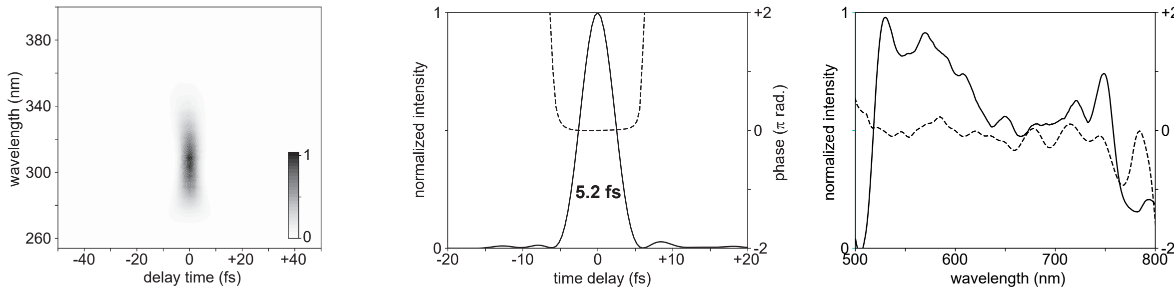

FIG. 12: Pulse characterization. (left) Measured SHG-FROG dataset. A generic Gaussian fit of the integrated signal gives a rough estimated pulse duration of 6.6 fs. (middle) Reconstructed temporal profile reveals a true pulse duration of 5.2 fs. (right) Reconstructed spectral profile of the pulse. Dashed lines are the phase profiles.

To measure the pulse duration, we use the second-harmonic generation, frequency-resolved optical gating (SHG-FROG) method.[56] The SHG medium is a 10-μm thick BBO crystal cut to $\theta \sim 60^\circ$, which is the appropriate cut angle for a frequency of 500 THz (600 nm), which is roughly the central frequency of the pulse. A straightforward calculation shows that the crystal is thin enough to phase match the entire bandwidth. At a delay time of zero, the SHG signal spans from about 265 nm to about 390 nm, and we use an uncoated CaF_2 lens to refocus the SHG beam into a USB spectrometer designed for ultraviolet light. Many USB spectrometers incorporate optics having protected-silver coatings, but these coatings are not compatible with ultraviolet wavelengths below about 350 nm. Therefore, the USB spectrometer we use in the SHG-FROG setup (Broadcom AFBR-S20M2UV) incorporates optics having aluminum coatings. The USB spectrometer is mounted on a 3-axis manual translation stage (OptoSigma TSD-655SLUU) to avoid using any optics after the SHG crystal other than the single lens, which enhances efficiency. We did not, however, calibrate the spectral irradiance of the detector because it is challenging to find calibration sources for this range of ultraviolet wavelengths, and therefore the dataset shown in FIG. 12(a) is not corrected for that modulation. This dataset was acquired using a delay stage having a bidirectional repeatability of ±0.030 μm (Newport XMS50-S with XPS-D controller), which corresponds to ±0.1 fs. The reconstructed temporal and spectral profiles are shown in panels (b) and (c) of FIG. 12. Many authors have previously presented temporal profiles; the spectral profile is consistent with the understanding of pulse compression established by Shank and coworkers in the 1980s.[38]

We also use the detected spectrum from the ultraviolet USB spectrometer as the feedback signal in the pulse-shaper's evolutionary optimization algorithm,[57] which has a significant speed advantage compared to our prior works that used a visible-wavelength signal arising from TG-FROG as the feedback, because those works used a CCD-based spectrometer that had a slow acquisition rate.[55,58] Currently, we can display a pattern on the deformable mirror (OKO Tech linear, aluminum coated, 40-channel MMDM) and detect the SHG signal at a rate of about 20 Hz. The deformable mirror is based on micro-mechanical technology, and it has much less hysteresis and a faster update rate than piezoelectric-based deformable mirrors.

B. Nonresonant Response

One issue that plagues time-resolved spectroscopy measurements is the large nonresonant response arising from the solvent and cuvette windows. Sometimes called a 'coherent artifact' or a 'coherence spike', this undesired signal primarily arises from the Kerr effect in which the presence of a high-field-strength pump pulses adds a nonlinear term to the refractive index of the material.[59] All else being equal, a decrease in the pulse duration will increase the field strength, which will subsequently increase the Kerr effect signal. Hence, even with 5-fs duration pulses acting as both pump and probe, the nonresonant response can dominate the early-time dynamics and persist beyond the pulse duration. In prior works, we were able to achieve measurements in which the nonresonant response is less than half of the total signal at time zero and disappears by 30 fs by minimizing the thickness of the cuvette windows and increasing the concentration of the sample to reduce the sample pathlength as much as possible.[60] Wire-guided jets that eliminate the cuvette windows also have this advantage.[50–52] Measurements on single-crystal samples that do not require a cuvette or solvent show no detectable nonresonant response.[49]

Prior researchers have accounted for the nonresonant response by modeling and fitting it

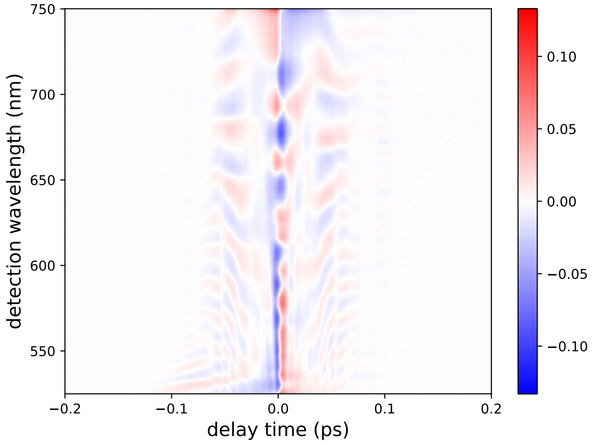

FIG. 13: Signal produced by a 1-mm thick Infrasil window. The ∼5-fs duration of the pump and probe pulses yields, via the Kerr effect, non-negligible nonresonant response.

as a linear combination of a Gaussian profile along with multiple derivatives of the Gaussian profile.[61–65] Recent work has shown that neural networks can be used to model and remove the nonresonant response as well.[66] FIG. 13 shows the signal arising from a 1-mm thick Infrasil window. The measurement shows the expected abrupt response directly at time zero, and non-negligible wings that extend to about ±50 fs. In this scan, there was a 'tail' in the blue; this is a common feature when the deformable-mirror algorithm has not converged completely. This problematic 'tail' can in some cases extend for several hundred femtoseconds, but fortunately it can be removed completely with more iterations of the compression algorithm.

C. Transient–Absorption Spectroscopy of Methylene Blue

To demonstrate the capabilities of the NOPA, we use it to produce both the pump and probe beams in a transient–absorption spectrometer having a crossing angle of $\sim 1^\circ$. We chose to measure the molecule methylene blue because prior work has detailed the molecular origins of the quantum-beat signals.[67] Methylene blue is structurally similar to the larger family of oxazine molecules, which are well studied in the context of quantum-beat measurements,[54,68–71] where the oxygen atom in the central ring of an oxazine is replaced by a sulfur atom in methylene blue.

FIG. 14 contains the transient–absorption spectrum as measured using the best practices

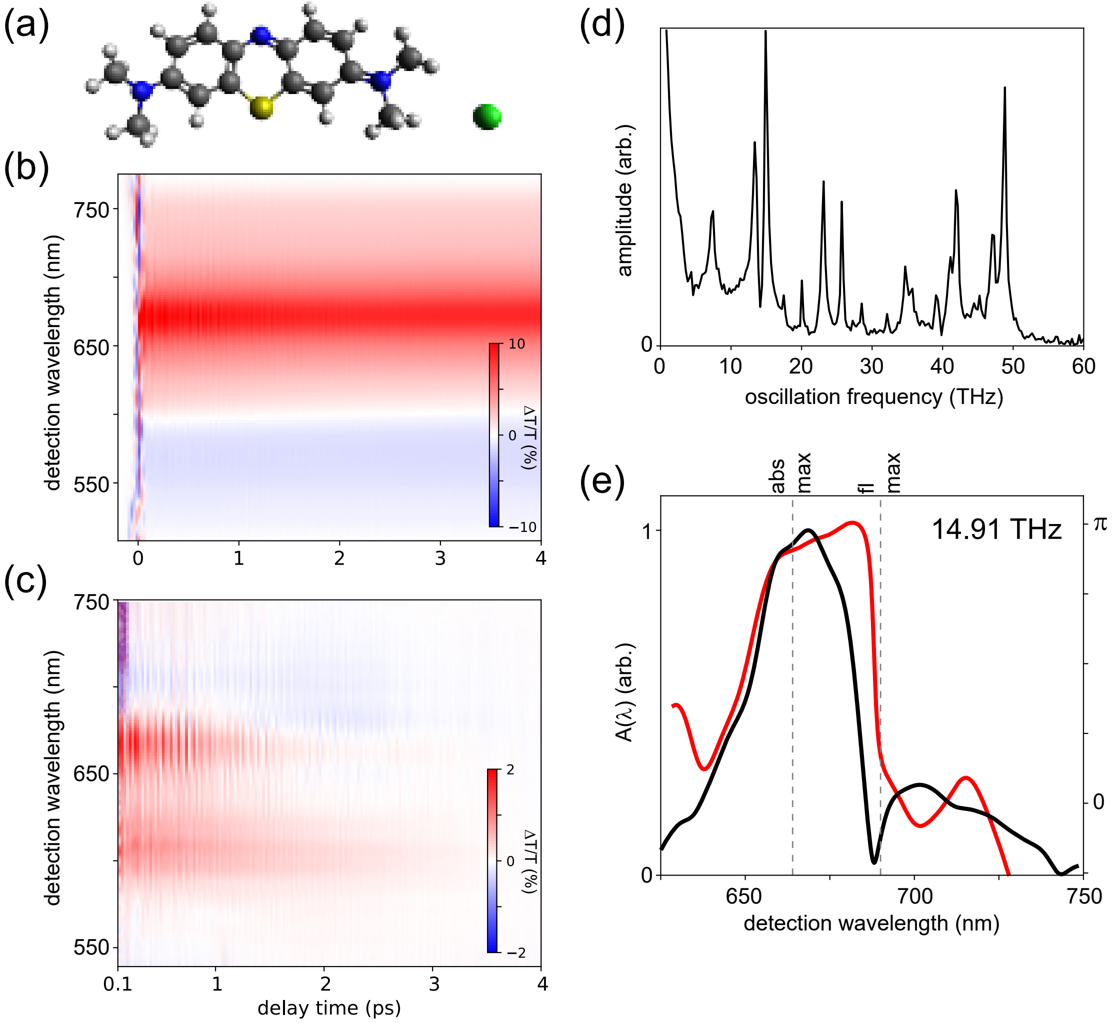

FIG. 14: Methylene blue (a) molecular structure, (b) raw transient–absorption spectrum, (c) spectrum with population decays removed, (d) 1D vibronic spectrum showing more than 15 distinct peaks, and (e) Femtosecond coherence spectrum (FCS) of the peak at 14.91 THz (497 cm^{-1}). Black and red lines represent the amplitude and phase profiles, respectively, and the dashed vertical lines indicate absorption and fluorescence maxima.

of shot-to-shot acquisitions, proper averaging mathematics, and balanced detection of the probe.[68] To isolate and study the quantum beats that arise from the molecular vibrational modes, we subtract a fit of a decaying exponential signal at each detection wavelength. Such quantum beats are very sensitive to the chirp on the pump pulse,[14,16] and therefore the efforts we have undertaken to minimize chirp are critical. The second panel in FIG. 14 shows that this adequately isolates the quantum beats. Fourier transformation creates a dataset of amplitude at each oscillation frequency as a function of detection wavelength. We then take the sum over all detection wavelengths of the absolute-value signal to yield a 1D vibronic spectrum, shown in third panel of FIG. 14. There are approximately 15 peaks in this spectrum at frequencies of 3.4, 7.3, 13.4, 14.9, 17.5, 20.0, 23.1, 25.7, 28.5, 32.1, 34.7, 35.7, 39.1, 41.1, 41.9, 47.0, and 48.8 THz, which correspond, respectively, to 113, 244, 447, 497, 584, 667, 771, 857, 951, 1071, 1157, 1191, 1304, 1371, 1398, 1568, and 1628 cm^{-1}. Dean *et al.* in prior work.[67] detailed the molecular origins of these modes, some of which are overtones and combination bands. Because of the increase in bandwidth of our pump pulse relative to the pump pulse used in that 2015 report, the high-frequency modes are no longer suppressed in the 1D vibronic spectrum.

Finally we present in the bottom panel of FIG. 14 a femtosecond coherence spectrum (FCS) for the oscillations that occur at a frequency of 14.9 THz (497 cm^{-1}). The FCS contains a black line indicating the relative amplitude of the oscillations as a function of detection wavelength, $A(\lambda)$, while the red line contains the corresponding phase function, $\phi(\lambda)$. The FCS shows a dramatic amplitude node and a corresponding phase shift of almost exactly π at a wavelength of 689 nm, which is within calibration error (± 1 nm) of the wavelength of maximum fluorescence (690 nm). Literature reports have established that an FCS with an amplitude node and π phase shift at the fluorescence maximum is indicative that the vibrational wavepacket oscillations occured on the excited-state potential-energy surface, not the ground-state potential-energy surface.[69,72–77] The latter would have given rise to an amplitude node and π phase shift at the absorption maximum. Therefore, the measured FCS presented in the bottom panel of FIG. 14 indicate that ultrabroadband pulses that encompass the sample absorption spectrum do suppress ground-state vibrational quantum beats and isolate excited-state vibrational wavepackets.

V. CONCLUSIONS & OUTLOOK

Due to the scientific need to conduct time-resolved spectroscopy measurements of a wider range of condensed-phase samples,[13,78,79] researchers continue to refine instrumentation to yield femtosecond pulses having ever increasing bandwidths while maintaining key laser properties such as low shot-to-shot fluctuations and an excellent spatial mode. The perceived complexity of NOPAs has led some researchers to choose high-power supercontinuum generation as an ultrabroadband light source to conduct time-resolved spectroscopy measurements.[80–84] Those prior reports indicate that, relative to what is possible with a NOPA, high-power supercontinuum sources typically have substantially higher ($\geq$2%) shot-to-shot fluctuations and yield spectra that are not as broadband and less spectrally flat. The CPA-PFM-NOPA detailed in this manuscript includes modifications that are based on fundamental principles of spatiotemporal dispersion arising from the wavelength-dependent refractive index, $n(\lambda)$. The design incorporates a number of updates and improvements that increase bandwidth and robustness while simultaneously minimizing shot-to-shot fluctuations and enabling ease-of-use. In one instance, we included a second stage for increasing power and to further reduce fluctuations. This was a degenerate arrangement in which the pump-tilt angle and the crystal-cut angles were identical in both stages. The methods detailed herein are applicable to NOPAs operating with differing pump wavelengths, repetition rates, and amplification materials.

The outlook for further enhancements is modest. A nondegenerate multi-stage NOPA seemingly could allow for a bandwidth increase. We have made numerous attempts at nondegenerate amplification using two-stage NOPAs. For example, we attempted to use our standard NOPA output pulse as a seed for a second stage having crystal-cut and pump-tilt angles appropriate for amplification in the blue, similar to the conditions used for our rubrene work.[49] In principle this would have produced a pulse having a bandwidth from 460 nm to 800 nm. However, these attempts failed because of strong fluctuations in the overlap region of the spectrum arising from interference effects. The technical workarounds we attempted did not resolve the interference issue. If this issue were to be resolved, one could envision almost unlimited bandwidth possible from a multi-stage NOPA. A second avenue that may allow for further enhancements is the identification and production of an amplification medium that is superior to BBO. Such a novel material would need to be as robust as BBO but have improved ordinary and extraordinary indices of refraction.

SUPPLEMENTARY MATERIAL

CAD files for the ‘chair’ mount used in the pump arm, the 1” diameter fixed mirror mount, and the adapter plate for mounting the OAPM.

AUTHOR INFORMATION

The authors have no conflicts to disclose.

DATA AVAILABILITY

The data that support the findings of this study are available from the corresponding author upon reasonable request.

ACKNOWLEDGEMENTS

The DOE, Office of Basic Energy Sciences, Division of Materials Science and Engineering through the Established Program to Stimulate Competitive Research (EPSCoR), via award No. DE-SC0020089 supported the research at Boise State University.

Appendix: Measurement, Analysis, and Minimization of Pulsed-Laser Fluctuations

Pulsed lasers suffer from shot-to-shot fluctuations that are detrimental to measurements, and therefore it is critical to measure, analyze, and minimize the fluctuations. To measure the fluctuations, we need optoelectronics instrumentation that faithfully converts the intensity of each laser shot at kHz repetition-rate lasers into a voltage measurable on the computer. Our implementation is an updated version of that reported elsewhere[85–87] in which the optoelectronics package consists of a silicon photodiode, current preamplifier for transformation of the weak photocurrent to a detectable voltage, and a data-acquisition (DAQ) board for digitization of the signals on the computer. In this contribution, we report data measured using a photodiode with an on-board current amplifier (New Focus 2001-FS). The on-board current preamplifier reduces noise relative to previous implementations that incorporated an external current preamplifier.[54,68,87] The DAQ (NI PCI-6281) offers 18-bit resolution and the ability to both 'clock' and 'trigger' the acquisitions, where the former is a transistor–transistor logic (TTL) signal from the source laser—timed to microsecond accuracy to coincide with the transient electrical signal arriving from the current preamplifier—that serves to synchronize the digitization process for each acquisition with

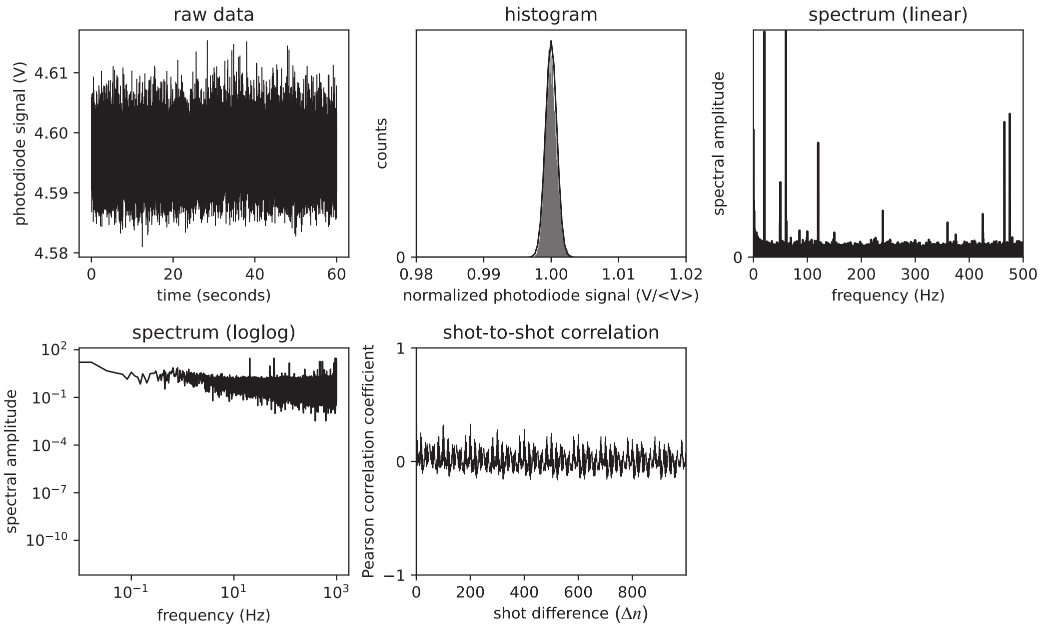

FIG. 15: Example analysis of 1-kHz Ti:sapphire laser fluctuations, where the RSD was ~0.08%. The analysis methods yield information on laser alignment, environmental sources of fluctuations, and also information on the number of shots required for convergence of averaged values.

high accuracy and the latter serves to initiate a set of acquisitions. The pulse-intensity measurement yields a set of voltage values with inherent noise level well below the level of the laser noise.[86] Two robust initial methods to assess the implementation of an optoelectronics package are (1) to ensure that blocking the beam near the source generates a value of ~0 V and (2) that temporarily adding an ND 0.3 filter before the detector reduces the voltage by half.

There are several useful methods to analyze fluctuations for a set of N intensity values, $I(N)$. It is productive to consider the intensity of pulse n as $I_n = I\,(1+\delta_n)$, where I is the average intensity and δ_n is the normalized fluctuation. An important quantitative metric is the relative standard deviation (RSD), RSD $= \sigma_I/\overline{I}$, where σ_I and $\overline{I}$ are the standard deviation and mean, respectively, of the N measured intensity values (voltages). The RSD reports on the normalized variance in the measurement, which is the appropriate method to quantify the fluctuations.[88] A well-aligned kHz Ti:sapphire amplified laser can have an RSD of less than 0.1%. For example the RSD of the dataset displayed in FIG. 15 is 0.08%. A second method is to inspect a histogram of the normalized voltage signals. A well-aligned laser will be symmetric about the average value. Misalignment or detector saturation issues can lead to a skew or sharp cut-off, respectively. The third and fourth useful analysis methods arise from computation of the noise spectrum via fast Fourier transformation, $A(\nu_N) = \mathcal{F}[I(N)]$. A laser-noise spectrum typically displays high-frequency fluctuations arising from the harmonics of the electrical power system and—when plotted on a logarithmic scale—may show low-frequency fluctuations due to duty cycling of thermal-control systems. Indeed, the two spectra in FIG. 15 show about 10 discrete high-frequency peaks, most of which are the fundamental electrical frequency (60 Hz) and its harmonics. The fifth quantification method is to compute the Pearson correlation coefficient

$$C(\Delta n) = \frac{\text{cov}[\sigma_n, \sigma_{n+\Delta n}]}{(\sigma_n)^2}, \tag{A.1}$$

where the covariance function is used in the numerator and where we assume in the denominator that $\sigma_n = \sigma_{n+\Delta n}$ for a series of pulse differences that is much less than the size of the overall dataset, $\Delta n \ll N$. Such a plot quantifies the correlation between the intensity of pulse n to pulse $n + \Delta n$, where $0 \leq \Delta n \leq 1000$ for $N = 60000$ in FIG. 15. By definition of the covariance function, $C(0) = 1$, and this is the case for the representative dataset used here. Some authors have constructed spectrometers that use sequential shots (n and $n+1$) for noise-reduction schemes and therefore desired that the correlation remain high for $\Delta n > 0$. However, one must be careful to average over a large number of shots in such cases so that the average converges to the true value without an offset.[68] By contrast, when using shot-by-shot (n only) balanced-detection schemes, one desires that the correlation drop to 0 immediately after $\Delta n = 0$ to reach a correctly converged value with the fewest number of shots.

The stability of a NOPA is ultimately bounded by the stability of the source laser, whose stability, in turn, is bounded by the laboratory environment. A key optimization is to identify and remove environmental noise sources because they can lead to oscillations or drift. Common examples are electrical noise and thermal-control systems. The first step to minimizing these noise sources is identification. We typically measure the shot-to-shot stability of the kHz commercial amplifier on short-term (∼10 second) and long-term (∼1-hour) timescales. Using this approach, we have detected environmentally induced fluctuations of the laser intensity as high as 5% and minimized them to ∼0.1%. Ways to minimize the discrete peaks arising from electrical noise include passive bandpass or edgepass electrical filters as well as medical-grade isolation transformers on laser power supplies. Another method to reduce high-frequency fluctuations for kHz Ti:sapphire amplifiers is that many yttrium lithium fluoride (YLF) pump lasers were designed to operate with the highest stability at a repetition rate of 5 kHz. If other electronics or sample-pumping considerations prevent operation at 5 kHz, one can still run the pump laser at 5 kHz but switch the Pockels cell at an integer value divisor. We have empirically found this method to decrease shot-to-shot fluctuations in some cases. Finally, minimization of oscillations due to thermal-control duty cycles typically involves changes to the temperature set points, fluid volumes, and the parameters of proportional–integral–derivative (PID) controller loops. The fluctuations arising from thermal-control noise are typically lower-frequency components that only appear on the $\sim$1-hour time scans.

Measuring the power of the amplified laser to identify and remove noise sources can be very productive, but power fluctuations are only one possible problem caused by environmental noise. Changes in temperature and humidity can also cause fluctuations in the pulse duration, primarily caused by small but significant pathlength changes in 4-f stretchers and compressors. Therefore, we also measure a second-harmonic beam using a BBO crystal and a polarizer or bandpass filter to redirect the residual fundamental. It can be extremely informative to measure—using two separate photodiodes with onboard current preamplifiers running to distinct channels of the same DAQ—the fundamental and second-harmonic signals simultaneously and thereby distinguish pulse-duration fluctuations from pulse-intensity fluctuations. A common source of pulse-duration fluctuations is variation in temperature inside and outside an amplified Ti:sapphire laser enclosure, which sets up convection currents. One method to reduce this problem is to tightly seat a thick ($\sim$2 inch) piece of rigid foam insulation on top of the exterior of the laser enclosure and wait for thermal equilibrium to be reached.

Mechanical fluctuations are the final source of noise to discuss. Minimizing these fluctuations begins at the construction and design phase of a laboratory, where one should use the thickest possible table(s) and ideally choose a table that is large enough such that the entire setup—from source laser to detector—is on a single table. In addition, during construction of a spectrometer and NOPA, we have found it very helpful to maximize the number of fixed mounts. In our experience, each adjustable knob of a kinematic mirror mount adds a small amount of mechanical instability, and therefore removing as many as possible increases stability. To identify mounts that have significant individual instability, one can monitor a signal of interest while conducting two tests. The first is to blow a puff of air onto the back surface of an optic using a bulb blower and assess the amount of change in the signal. The second is to press slowly but firmly onto the surface of the table directly adjacent to the base of the mount, again while monitoring the signal for variations. Typically, only a handful of mounts are significant at an individual level, however, the accumulated stability increase upon replacing several kinematic mirror mounts with fixed mounts can be quite consequential. In some cases, we have found commercial fixed mounts to remain unstable; in such cases, we use a custom fixed mirror mount machined from 303 stainless steel rather than aluminum. We include a computer-aided design .step file for this 1-inch diameter fixed mount as Supplementary Material.

REFERENCES

[1] G. M. Gale, M. Cavallari, T. J. Driscoll, and F. Hache, "Sub-20-fs tunable pulses in the visible from an 82-MHz optical parametric oscillator," Opt. Lett. **20**, 1562–1564 (1995).

[2] T. Wilhelm, J. Piel, and E. Riedle, "Sub-20-fs pulses tunable across the visible from a blue-pumped single-pass noncollinear parametric converter," Opt. Lett. **22**, 1494–1497 (1997).

[3] G. Cerullo, M. Nisoli, S. Stagira, and S. De Silvestri, "Sub-8-fs pulses from an ultrabroadband optical parametric amplifier in the visible," Opt. Lett. **23**, 1283–1285 (1998).

[4] A. Shirakawa and T. Kobayashi, "Noncollinearly phase-matched femtosecond optical parametric amplification with a 2000 cm^{-1} bandwidth," Appl. Phys. Lett. **72**, 147–149 (1998).

[5] A. Shirakawa, I. Sakane, M. Takasaka, and T. Kobayashi, "Sub-5-fs visible pulse generation by pulse-front-matched noncollinear optical parametric amplification," Appl. Phys. Lett. **74**, 2268–2270 (1999).

[6] M. Zavelani-Rossi, G. Cerullo, S. De Silvestri, L. Gallmann, N. Matuschek, G. Steinmeyer, U. Keller, G. Angelow, V. Scheuer, and T. Tschudi, "Pulse compression over a 170-THz bandwidth in the visible by use of only chirped mirrors," Opt. Lett. **26**, 1155–1157 (2001).

[7] P. Tzankov, I. Buchvarov, and T. Fiebig, "Broadband optical parametric amplificiation in the near UV-VIS," Optics Communications **203**, 107–113 (2002).

[8]T. Fuji, T. Saito, and T. Kobayashi, "Dynamical observation of Duschinksy rotation by sub-5-fs real-time spectroscopy," Chem. Phys. Lett. **332**, 324–330 (2000).

[9]D. Polli, P. Altoe, O. Weingart, K. M. Spillane, C. Manzoni, D. Brida, G. Tomasello, G. Orlandi, P. Kukura, R. A. Mathies, M. Garavelli, and G. Cerullo, "Conical intersection dynamics of the primary photoisomerization event in vision," Nature **467**, 440–443 (2010).

[10]P. J. M. Johnson, A. Halpin, T. Morizumi, V. I. Prokhorenko, O. P. Ernst, and R. J. D. Miller, "Local vibrational coherences drive the primary photochemistry of vision," Nature Chemistry **7**, 980–986 (2015).

[11]D. B. Turner, R. Dinshaw, K.-K. Lee, M. S. Belsley, K. E. Wilk, P. M. G. Curmi, and G. D. Scholes, "Quantitative investigations of quantum coherence for a light-harvesting protein at conditions simulating photosynthesis," Phys. Chem. Chem. Phys. **14**, 4857–4874 (2012).

[12]A. Halpin, P. J. M. Johnson, R. Tempelaar, R. S. Murphy, J. Knoester, T. L. C. Jansen, and R. Miller, "Two-dimensional spectroscopy of a molecular dimer unveils the effects of vibronic coupling on exciton coherences," Nature Chemistry **6**, 196–201 (2014).

[13]B. K. Petkov, T. A. Gellen, C. A. Farfan, W. P. Carbery, B. E. Hetzler, D. Trauner, X. Li, W. J. Glover, D. J. Ulness, and D. B. Turner, "Two-dimensional electronic spectroscopy reveals the spectral dynamics of Förster resonance energy transfer," Chem **5**, 1–15 (2019).

[14]C. J. Bardeen, Q. Wang, and C. V. Shank, "Selective excitation of vibrational wave packet motion using chirped pulses," Phys. Rev. Lett. **75**, 3410–3413 (1995).

[15]G. Cerullo, C. J. Bardeen, Q. Wang, and C. Shank, "High-power femtosecond chirped pulse excitation of molecules in solution," Chem. Phys. Lett. **262**, 362–368 (1996).

[16]C. Bardeen, Q. Wang, and C. Shank, "Femtosecond chirped pulse excitation of vibrational wave packets in LD690 and bacteriorhodopsin," J. Phys. Chem. A **102**, 2759–2766 (1998).

[17]V. I. Klimov and D. W. McBranch, "Femtosecond high-sensitivity, chirp-free transient absorption spectroscopy using kilohertz lasers," Opt. Lett. **23**, 277–279 (1998).

[18]S. Malkmus, R. Durr, C. Sobotta, H. Pulvermacher, W. Zinth, and M. Braun, "Chirp dependence of wave packet motion in oxazine 1," J. Phys. Chem. A **109**, 10488–10492 (2005).

[19]P. F. Tekavec, J. A. Myers, K. L. M. Lewis, F. D. Fuller, and J. P. Ogilvie, "Effects of chirp on two-dimensional Fourier transform electronic spectra," Opt. Express **18**, 11015–11024 (2010).

[20] N. Christensson, Y. Avlasevich, A. Yartsev, K. Müllen, T. Pascher, and T. Pullerits, "Weakly chirped pulses in frequency resolved coherent spectroscopy," J. Chem. Phys. **132**, 174508 (2010).

[21] A. Wand, S. Kallush, O. Shoshanim, O. Bismuth, R. Kosloff, and S. Ruhman, "Chirp effects on impulsive vibrational spectroscopy: A multimode perspective," Phys. Chem. Chem. Phys. **12**, 2149–2163 (2010).

[22] A. Giree, M. Mero, G. Arisholm, M. J. J. Vrakking, and F. J. Furch, "Numerical study of spatiotemporal distortions in noncollinear optical parametric chirped-pulse amplifiers," Opt. Express **25**, 3104–3121 (2017).

[23] P. J. M. Johnson, V. I. Prokhorenko, and R. J. D. Miller, "Enhanced bandwidth noncollinear optical parametric amplification with a narrowband anamorphic pump," Opt. Lett. **36**, 2170–2072 (2011).

[24] A. Baltuška, T. Fuji, and T. Kobayashi, "Visible pulse compression to 4 fs by optical parametric amplification and programmable dispersion control," Opt. Lett. **27**, 306–308 (2002).

[25] J. Limpert, C. Aguergaray, S. Montant, I. Manek-Hönninger, S. Petit, D. Descamps, E. Cormier, and F. Salin, "Ultra-broad bandwidth parametric amplification at degeneracy," Opt. Express **13**, 7386–7392 (2005).

[26] G. Arisholm, J. Biegert, P. Schlup, C. Hauri, and U. Keller, "Ultra-broadband chirped-pulse optical parametric amplifier with angularly dispersed beams," Opt. Express **12**, 518–530 (2004).

[27] C. Aguergaray, O. Schmidt, J. Rothhardt, D. Schimpf, D. Descamps, S. Petit, J. Limpert, and E. Cormier, "Ultra-wide parametric amplification at 800 nm toward octave spanning," Opt. Express **17**, 5153–5162 (2009).

[28] L. Cardoso, H. Pires, and G. Figueira, "Increased bandwidth optical parametric amplification of supercontinuum pulses with angular dispersion," Opt. Lett. **34**, 1369–1371 (2009).

[29] D. Herrmann, C. Homann, R. Tautz, M. Scharrer, P. S. Russell, F. Krausz, L. Veisz, and E. Riedle, "Approaching the full octave: Noncollinear optical parametric chirped pulse amplification with two-color pumping," Opt. Express **18**, 18752–18762 (2010).

[30] S. Adachi, Y. Watanabe, Y. Sudo, and T. Suzuki, "Few-cycle pulse generation from noncollinear optical parametric amplifier with static dispersion compensation," Chem.

Phys. Lett. **683**, 7–11 (2017).

[31]J. Bromage, C. Dorrer, and J. Zuegel, "Angular-dispersion-induced spatiotemoral aberrations in noncollinear optical parametric amplifiers," Optics Letters **35**, 2251–2253 (2010).

[32]J. Bromage, J. Rothhardt, S. Hädrich, C. Dorrer, C. Jocher, S. Demmler, J. Limpert, A. Tünnermann, and J. D. Zuegel, "Analysis and suppression of parasitic process in noncollinear optical parametric amplifiers," Optics Express **19**, 16797–16808 (2011).

[33]A. Zaukevičius, V. Jukna, R. Antipenkov, V. Martinėnaitė, A. Varanavičius, A. P. Piskarskas, and G. Valiulis, "Manifestation of spatial chirp in femtosecond noncollinear optical parametric chirped-pulse amplifier," J. Opt. Soc. Am. B **28**, 2902–2908 (2011).

[34]G. Cerullo and S. De Silvestri, "Ultrafast optical parametric amplifiers," Rev. Sci. Instr. **74**, 1–18 (2003).

[35]C. Manzoni and G. Cerullo, "Design criteria for ultrafast optical parametric amplifiers," J. Opt. **18**, 103501 (2016).

[36]R. W. Boyd, *Nonlinear Optics*, 2nd ed. (Academic Press, San Diego, 2003).

[37]E. Hecht, *Optics*, 5th ed. (Pearson, 2016).

[38]R. L. Fork, C. H. Brito Cruz, P. C. Becker, and C. V. Shank, "Compression of optical pulses to six femtoseconds by using cubic phase compensation," Opt. Lett. **12**, 483–485 (1987).

[39]J. Stewart, *Calculus: Early Transcendentals*, 8th ed. (Cengage Learning, 2015).

[40]A. V. Smith, *Crystal Nonlinear Optics: With SNLO Examples*, 2nd ed. (AS-Photonics, Albuquerque, NM, USA, 2015).

[41]T. Kobayashi and A. Baltuška, "Sub-5 fs pulse generation from a noncollinear optical parametric amplifier," Meas. Sci. Technol. **13**, 1671–1682 (2002).

[42]S. Akturk, X. Gu, E. Zeek, and R. Trebino, "Pulse-front tilt caused by spatial and temporal chirp," Opt. Express **12**, 4399–4410 (2004).

[43]S. Akturk, X. Gu, P. Gabolde, and R. Trebino, "The general theory of first-order spatio-temporal distortions of Gaussian pulses and beams," Opt. Express **13**, 8642–8661 (2005).

[44]A. Dubietis, G. Jonušauskas, and A. Piskarskas, "Powerful femtosecond pulse generation by chirped and stretched pulse parametric amplification in BBO crystal," Opt. Commun. **88**, 437–440 (1992).

[45]P. Baum, M. Breuer, E. Riedle, and G. Steinmeyer, "Brewster-angled chirped mirrors for broadband pulse compression without dispersion oscillations," Opt. Lett. **31**, 2220–2222

(2006).

[46] L. Wang, G. Tóth, J. Hebling, and F. Kärtner, "Tilted-pulse-front schemes for terahertz generation," Laser Photonics Rev. **14**, 2000021 (2020).

[47] J. W. Goodman, *Introduction to Fourier Optics*, 3rd ed. (Roberts and Company Publishers, 2004).

[48] L. A. Bizimana, C. A. Farfan, J. Brazard, and D. B. Turner, "E to Z photoisomerization of phytochrome Cph1Δ exceeds the Born–Oppenheimer adiabatic limit," J. Phys. Chem. Lett. **10**, 3550–3556 (2019).

[49] I. Breen, R. Tempelaar, L. A. Bizimana, B. Kloss, D. R. Reichman, and D. B. Turner, "Triplet separation drives singlet fission after femtosecond correlated triplet pair production in rubrene," J. Am. Chem. Soc. **139**, 11745–11751 (2017).

[50] A. Picchiotti, V. I. Prokhorenko, and R. J. D. Miller, "A closed-loop pump-driven wire-guided flow jet for ultrafast spectroscopy of liquid samples," Rev. Sci. Instr. **86**, 093105 (2015).

[51] J. Lim, D. Paleček, F. Caycedo-Soler, C. N. Lincoln, J. Prior, H. von Berlepsch, S. F. Huelga, M. B. Plenio, D. Zigmantas, and J. Hauer, "Vibronic origin of long-lived coherence in an artificial molecular light harvester," Nat. Commun. **6**, 7755 (2015).

[52] A. Picchiotti, A. Nenov, A. Giussani, V. I. Prokhorenko, R. J. D. Miller, S. Mukamel, and M. Garavelli, "Pyrene, a test case for deep-ultraviolet molecular photophysics," J. Phys. Chem. Lett. **10**, 3481–3487 (2019).

[53] J. Schroeder, R. Mohr, C. J. Montrose, and P. B. Macedo, "Light scattering in a number of optical grade glasses," J. Non-Crystalline Solids **13**, 313–320 (1973/74).

[54] L. A. Bizimana, J. Brazard, W. P. Carbery, T. Gellen, and D. B. Turner, "Resolving molecular vibronic structure using high-sensitivity two-dimensional electronic spectroscopy," J. Chem. Phys. **143**, 164203 (2015).

[55] C. A. Farfan, J. Epstein, and D. B. Turner, "Femtosecond pulse compression using a neural-network algorithm," Optics Letters **43**, 5166–5169 (2018).

[56] R. Trebino, K. W. DeLong, D. A. Fittinghoff, J. N. Sweetser, M. A. Kumbugel, B. A. Richman, and D. J. Kane, "Measuring ultrashort laser pulses in the time-frequency domain using frequency-resolved optical gating," Rev. Sci. Instr. **68**, 3277–3296 (1997).

[57] T. Baumert, T. Brixner, V. Seyfried, M. Strehle, and G. Gerber, "Femtosecond pulse shaping by an evolutionary algorithm with feedback," Appl. Phys. B: Laser Optics **65**,

779–782 (1997).

[58] W. P. Carbery, A. Verma, and D. B. Turner, "Spin-orbit coupling drives femtosecond nonadiabatic dynamics in a transition metal compound," J. Phys. Chem. Lett. **8**, 1315–1322 (2017).

[59] R. R. Alfano, X. Q. Li, T. Jimbo, J. T. Manassah, and P. P. Ho, "Induced spectral broadening of a weak picosecond pulse in glass produced by an intense picosecond pulse," Opt. Lett. **11**, 626–628 (1986).

[60] T. Gellen, L. A. Bizimana, W. P. Carbery, I. Breen, and D. B. Turner, "Ultrabroadband two-quantum two-dimensional electronic spectroscopy," J. Chem. Phys. **145**, 064201 (2016).

[61] M. Lorenc, M. Ziolek, R. Naskrecki, J. Karolczak, J. Kubicki, and A. Maciejewski, "Artifacts in femtosecond transient absorption spectroscopy," Appl. Phys. B **74**, 19–27 (2002).

[62] A. L. Dobryakov, S. A. Kovalenko, and N. P. Ernsting, "Electronic and vibrational coherence effects in broadband transient absorption spectroscopy with chirped supercontinuum probing," J. Chem. Phys. **119**, 988–1002 (2003).

[63] A. L. Dobryakov, S. A. Kovalenko, and N. P. Ernsting, "Coherent and sequential contributions to femtosecond transient absorption spectra of a rhodamine dye in solution," J. Chem. Phys. **123**, 044502 (2005).

[64] A. L. Dobryakov and N. P. Ernsting, "Lineshapes for resonant impulsive stimulated Raman scattering with chirped pump and supercontinuum pprobe pulses," J. Chem. Phys. **129**, 184504 (2008).

[65] I. H. M. van Stokkum, M. Kloz, D. Polli, D. Viola, J. Weiβenborn, E. Peerbooms, G. Cerullo, and J. T. M. Kennis, "Vibronic dynamics resolved by global and target analysis of ultrafast transient absorption spectra," J. Chem. Phys. **155**, 114113 (2021).

[66] A. Bresci, M. Guizzardi, C. M. Valensise, F. Marangi, F. Scotognella, G. Cerullo, and D. Polli, "Removal of cross-phase modulation artifacts in ultrafast pump–probe dynamics by deep learning," APL Photon. **6**, 076104 (2021).

[67] J. C. Dean, S. Rafiq, D. G. Oblinksy, E. Cassette, C. C. Jumper, and G. D. Scholes, "Broadband transient absorption and two-dimensional electronic spectroscopy of methylene blue," J. Phys. Chem. A **119**, 9098–9108 (2015).

[68] J. Brazard, L. A. Bizimana, and D. B. Turner, "Accurate convergence of transient-absorption spectra using pulsed lasers," Rev. Sci. Instr. **86**, 053106 (2015).

[69] J. Brazard, L. A. Bizimana, T. Gellen, W. P. Carbery, and D. B. Turner, "Experimental detection of branching at a conical intersection in a highly fluorescent molecule," J. Phys. Chem. Lett. **7**, 14–19 (2016).

[70] J. Lu, Y. Lee, and J. M. Anna, "Extracting the frequency-dependent dynamic Stokes shift from two-dimensional electronic spectra with prominent vibrational coherences," J. Phys. Chem. B **124**, 8857–8867 (2020).

[71] M. S. Barclay, J. S. Huff, R. D. Pensack, P. H. Davis, W. B. Knowlton, B. Yurke, J. C. Dean, P. C. Arpin, and D. B. Turner, "Characterizing mode anharmonicity and Huang–Rhys factors using models of femtosecond coherence spectra," J. Phys. Chem. Lett. **13**, 5413–5423 (2022).

[72] W. T. Pollard and R. A. Mathies, "Analysis of femtosecond dynamic absorption spectra of nonstationary states," Annu. Rev. Phys. Chem. **43**, 497–523 (1992).

[73] Y. Tanimura and S. Mukamel, "Temperature dependence and non-Condon effects in pump-probe spectroscopy in the condensed phase," J. Opt. Soc. Am. B **10**, 2263–2268 (1993).

[74] D. M. Jonas, S. E. Bradforth, S. A. Passino, and G. R. Fleming, "Femtosecond wavepacket spectroscopy: Influence of temperature, wavelength, and pulse duration," J. Phys. Chem. **99**, 2594–2608 (1995).

[75] M. Liebel, C. Schnedermann, T. Wende, and P. Kukura, "Principles and applications of broadband impulsive vibrational spectroscopy," J. Phys. Chem. A **119**, 9506–9517 (2015).

[76] D. B. Turner and P. C. Arpin, "Basis set truncation further clarifies vibrational coherence spectra," Chem. Phys. **539**, 110948 (2020).

[77] P. C. Arpin and D. B. Turner, "Signatures of vibrational and electronic quantum beats in femtosecond coherence spectra," J. Phys. Chem. A **125**, 2425–2435 (2021).

[78] F. D. Fuller and J. P. Ogilvie, "Experimental implementations of two-dimensional Fourier transform electronic spectroscopy," Ann. Rev. Phys. Chem. **66**, 667–690 (2015).

[79] J. C. Wright, "Analytical chemistry, multidimensional spectral signatures, and the future of coherent multidimensional spectroscopy," Chem. Phys. Lett. **662**, 1–13 (2016).

[80] B. Spokoyny, C. J. Koh, and E. Harel, "Stable and high-power few cycle supercontinuum for 2D ultrabroadband electronic spectroscopy," Opt. Lett. **40**, 1014–1017 (2015).

[81] X. Ma, J. Dostál, and T. Brixner, "Broadband 7-fs diffractive-optic-based 2d electronic spectroscopy using hollow-core fiber compression," Opt. Express **24**, 20781–20791 (2016).

[82] C. Sonnichsen, P. Brosseau, C. Reid, and P. Kambhampati, "OPA-driven hollow-core

fiber as a tunable, broadband source for coherent multidimensional spectroscopy," Opt. Express **29**, 28352 (2021).

[83]S. M. Hart, W. J. Chen, J. L. Banal, W. P. Bricker, A. Dodin, L. Markova, Y. Vyborna, A. P. Willard, R. Haner, M. Bathe, and G. Schlau-Cohen, "Engineering couplings for exciton transport using synthetic DNA scaffolds," Chem **7**, 1–22 (2021).

[84]A. Kumar, P. Malevich, L. Mewes, S. Wu, J. P. Barham, and J. Hauer, "Transient absorption spectroscopy based on uncompressed hollow core fiber white light proves pre-association between a radical ion photocatalyst and substrate," J. Chem. Phys. **158**, 144201 (2023).

[85]C. Schriever, S. Lochbrunner, E. Riedle, and D. J. Nesbitt, "Ultrasensitive ultraviolet-visible 20 fs absorption spectroscopy of low vapor pressure molecules in the gas phase," Rev. Sci. Instr. **79**, 013107 (2008).

[86]C. A. Werley, S. M. Teo, and K. A. Nelson, "Pulsed laser noise analysis and pump-probe signal detection with a data acquisition card," Rev. Sci. Instr. **82**, 123108 (2011).

[87]S. D. McClure, D. B. Turner, P. C. Arpin, T. Mirkovic, and G. D. Scholes, "Coherent oscillations in the PC577 cryptophyte antenna occur in the excited electronic state," J. Phys. Chem. B **118**, 1296–1308 (2014).

[88]J. R. Taylor, *An Introduction to Error Analysis: The Study of Uncertainties in Physical Measurements*, 2nd ed. (University Science Books, 1997).